JGR Atmospheres

RESEARCH ARTICLE
10.1029/2023JD038487

Changes in Stratosphere-Troposphere Exchange of Air Mass and Ozone Concentration in CCMI Models From 1960 to 2099

Mingcheng Wang[1] and **Qiang Fu**[1]

[1]Department of Atmospheric Sciences, University of Washington, Seattle, WA, USA

Key Points:

- Global ozone stratosphere-troposphere exchange (STE) trends from Chemistry Climate Model Initiative models are −2.7% decade^{-1} for 1960–2000, and 4.7% decade^{-1} for 2000–2099 in RCP6.0 scenario
- For 1960–2000, a decreased global ozone STE magnitude was caused by ozone-depleting substance (ODS)-induced ozone loss, partly compensated by climate-induced changes
- For 2000–2099, climate-induced changes and phaseout of ODS contribute about two-thirds and one-third of the global ozone STE magnitude increase, respectively

Supporting Information:

Supporting Information may be found in the online version of this article.

Correspondence to:

Q. Fu,
qfu@uw.edu

Citation:

Wang, M., & Fu, Q. (2023). Changes in stratosphere-troposphere exchange of air mass and ozone concentration in CCMI models from 1960 to 2099. *Journal of Geophysical Research: Atmospheres*, *128*, e2023JD038487. https://doi.org/10.1029/2023JD038487

Received 3 JAN 2023
Accepted 22 JUN 2023

Abstract This study investigates changes in stratosphere-troposphere exchange (STE) of air masses and ozone concentrations from 1960 to 2099 using multiple model simulations from Chemistry Climate Model Initiative (CCMI) under climate change scenario RCP6.0. We employ a lowermost stratosphere mass budget approach with dynamic isentropic surfaces fitted to the tropical tropopause as the upper boundary of lowermost stratosphere. The multi-model mean (MMM) trends of air mass STEs are all small over all regions, which are within 0.3 (0.1) % decade^{-1} for 1960–2000 (2000–2099). The MMM trends of ozone STE for 1960–2000 are 0.3%, −2.7%, 3.4%, −0.9%, and −2.7% decade^{-1} over the Northern hemisphere (NH) extratropics, Southern hemisphere (SH) extratropics, tropics, extratropics, and globe, respectively. The corresponding ozone STE trends for 2000–2099 are 3.0%, 4.3%, 0.8%, 3.5%, and 4.7% decade^{-1}. Changes in ozone STEs are dominated by ozone concentration changes, driven by climate-induced changes and ozone-depleting substance (ODS) changes. For 1960–2000, small changes in ozone STEs in the NH extratropics are due to a cancellation between effects of climate-induced changes and ODS increases, while the ODS effect dominates in the SH extratropics, leading to a large ozone STE magnitude decrease. Increased ozone transport from tropical troposphere to stratosphere for 1960–2000 is due to increased tropospheric ozone. A decreased global ozone STE magnitude for 1960–2000 was largely caused by ODS-induced ozone loss that is partly compensated by climate-induced ozone changes. For 2000–2099, about two-thirds of global ozone STE magnitude increases are caused by ozone increases in the extratropical lower stratosphere due to climate-induced changes. The remaining one-third is caused by ozone recovery due to the phaseout of ODS.

Plain Language Summary Stratosphere-troposphere exchange (STE) of ozone is an important source of tropospheric ozone and can impact the tropospheric air quality. This study investigates changes in STE of ozone concentrations for 1960–2099 using multiple climate model simulations from the Chemistry Climate Model Initiative under the RCP6.0 scenario. It is shown that the trends in global ozone STEs are −2.7% decade^{-1} for 1960–2000, and 4.7% decade^{-1} for 2000–2099 in. In other words, global ozone STEs are decreased by 11% from 1960 to 2000, but increased by 47% from 2000 to 2099. We separate the contributions from climate change and ozone-depleting substance (ODS) effects to the ozone STE changes. A decreased global ozone STE magnitude for 1960–2000 was caused by ODS-induced ozone loss that is partly compensated by climate-induced ozone changes. For 2000–2099, about two-thirds of the global ozone STE magnitude increases are caused by ozone increases in the extratropical lower stratosphere due to climate changes. The remaining one-third is caused by ozone recovery due to the phaseout of ODS.

1. Introduction

Stratosphere-troposphere exchange (STE) of ozone is an important source for the tropospheric ozone budget (e.g., Bates & Jacob, 2020; Collins et al., 2003; Griffiths et al., 2020; Stohl et al., 2003). Bates and Jacob (2020) examined an expanded odd oxygen family and showed a greater stratospheric ozone contribution of up to 26% to the tropospheric ozone budget under present-day conditions in the GEOS-Chem model. In addition, ozone STE could impact tropospheric air quality, oxidation capacity, and methane lifetime (e.g., Fiore et al., 2002; Geng et al., 2017; Kentarchos & Roelofs, 2003; Lin et al., 2015; Ordóñez et al., 2007).

In response to greenhouse gas-induced climate changes, climate models consistently predict an acceleration of Brewer-Dobson circulation (BDC) (e.g., Abalos et al., 2021; Butchart, 2014; Butchart et al., 2006; Fu et al., 2010; Fu et al., 2019; Li et al., 2008; Lin et al., 2009; Lin & Fu, 2013) and increased ozone STEs (e.g., Abalos et al., 2020; Collins et al., 2003; Hegglin & Shepherd, 2009; Hess et al., 2015; Meul et al., 2018). Induced by anthropogenic ozone-depleting substances (ODS), the Antarctic ozone hole has been a focus of attention over

four decades (Molina & Rowland, 1974; Solomon et al., 1986; Solomon, 1999, and references therein). Due to the worldwide phaseout of the production of ODS imposed by the Montreal Protocol and its amendments, the ozone layer is expected to recover in the middle of the 21st century (WMO, 2007). The evolutions of stratospheric ozone associated with the ODS changes could also impact the stratospheric ozone influxes into the troposphere (e.g., Hegglin & Shepherd, 2009; Meul et al., 2018; Shindell et al., 2006). For instance, Shindell et al. (2006) found that more than half of the tropospheric ozone increase since the preindustrial period was offset by reduced ozone STE due to stratospheric ozone depletion.

Various approaches have been developed to estimate ozone STEs (see Hsu et al., 2005; Schoeberl, 2004; Stohl et al., 2003; Wang et al., 2022; Wang & Fu, 2021; Yang et al., 2016). The lowermost stratosphere mass budget approach (e.g., Appenzeller et al., 1996) can be used to accurately quantify the net mass fluxes of air, ozone, and other chemical species across the tropopause over the Northern hemisphere (NH) extratropics, Southern hemisphere (SH) extratropics, tropics, and globe, although it cannot isolate STE events spatially and temporally. The mass budget approach is often used as an important constraint and reference to assess estimates from other methods (e.g., Stohl et al., 2003; Škerlak et al., 2014), and has been widely used to estimate air mass and ozone STEs in the past, current, and future climates (e.g., Hegglin & Shepherd, 2009; Meul et al., 2018; Schoeberl, 2004; Wang et al., 2022; Wang & Fu, 2021).

The 380 K isentropic surface, or 100 hPa, is often used as the upper boundary of the lowermost stratosphere in the mass budget approach (e.g., Appenzeller et al., 1996; Hegglin & Shepherd, 2009; Olsen et al., 2013; Schoeberl, 2004; Wang & Fu, 2021; Yang et al., 2016). However, this upper boundary is expected to change with the changing tropical tropopause in different climates. Previous studies also often only estimated the ozone stratosphere to troposphere transports and their changes over the extratropics (e.g., Hegglin & Shepherd, 2009; Meul et al., 2018). Based on reanalysis and observations, Wang and Fu (2021) found that tropical upward ozone flux compensates for a significant portion of extratropical downward ozone flux: the ozone STEs averaged over 2007–2010 are 535 and 350 Tg year^{-1} over the extratropics and globe, respectively. In investigating air mass and ozone STE changes in the Last Glacial Maximum (LGM) versus the preindustrial climate, Wang et al. (2022) introduced a dynamic isentropic surface that is determined by fitting to the tropical tropopause as the upper boundary of the lowermost stratosphere in the mass budget approach. This method is referred to as the dynamic upper isentrope method (Wang et al., 2022), which is particularly suitable for estimating air mass and ozone STEs across different climates. Wang et al. (2022) applied this method to the WACCM6 simulations of the LGM climate (Fu et al., 2020a, 2020b; Wang et al., 2020).

In this study, we investigate the changes in air mass and ozone STEs for 1960–2000 and 2000–2099 based on multiple Chemistry Climate Model Initiative (CCMI) model simulations (Morgenstern et al., 2017) by employing the dynamic upper isentrope method. The future climate simulations here follow the IPCC RCP6.0 scenario. The contributions to the air mass and ozone STE changes from the greenhouse gas and sea surface temperature (GHG/SST) changes and ODS changes are quantified. The roles of ozone STEs in tropospheric ozone budgets are also examined. This study differs from previous studies by (a) using a dynamic isentropic surface as the upper boundary of the lowermost stratosphere, and (b) estimating STEs of ozone concentrations not only over the extratropics but also over the globe including the entire tropical region. Note that ozone STE over the globe instead of that over the extratropics is the STE contribution to the tropospheric ozone budget (Wang & Fu, 2021).

The CCMI modeling data and analysis method used in this study are described in Section 2. Section 3 presents the air mass and ozone STE changes, while the causes for these STE changes are shown in Section 4, and Section 5 separates the GHG/SST and ODS contributions to the STE changes. Section 6 examines the tropospheric ozone budget. A comparison with previous studies is discussed in Section 7. A summary and conclusions are provided in Section 8.

2. Modeling Data and Analysis Method

Model simulations, including REF-C2, SEN-C2-fODS, and SEN-C2-fGHG, from the CCMI over 1960–2099, are used in this study (Table S1 in Supporting Information S1). In REF-C2 experiments, the historic forcings and observed sea surface conditions are used for 1960–2010; the 2010–2099 period follows the WMO (2010) A1 scenario for ODS and RCP 6.0 (Meinshausen et al., 2011) for other GHG, tropospheric ozone precursors, and aerosol and aerosol precursor emissions (Morgenstern et al., 2017). The simulation of SEN-C2-fODS is the same

as REF-C2, but with the ODS fixed to 1960 levels, while SEN-C2-fGHG is the same as REF-C2 but with GHGs fixed at 1960 levels and SST and sea ice conditions prescribed as the 1955–1964 average. In this study, the effect of GHG/SST changes is quantified as the difference between the REF-C2 and SEN-C2-fGHG, and the effect of ODS changes is the difference between REF-C2 and SEN-C2-fODS. Note that the GHG/SST effect here is the combined effects of GHG and SST/sea ice changes, and the latter includes those not only due to GHG changes but also other factors such as aerosol changes and internal variability. More details about the CCMI models and experiments can be found in Morgenstern et al. (2017).

In this study, we use simulations from 10 CCMI models for REF-C2 and from four models for SEN-C2-fODS and SEN-C2-fGHG (Table S1 in Supporting Information S1), which provide the required fields, including radiative heating rates, for our air mass and ozone STE calculations. Furthermore, we only analyze and present results based on the first ensemble of the model for which there are multiple ensemble members. The results, however, are almost identical if we use all ensemble members (not shown).

The monthly ERA5 and Modern-Era Retrospective Analysis for Research and Applications, version 2 (MERRA2) from 1980 to 2020 are used in this study. Compared to ERA-Interim, the representations of the atmospheric temperature, wind, and humidity are generally better in ERA5 (Hersbach et al., 2020). The representation of the stratosphere including ozone is improved in MERRA2 relative to MERRA (Gelaro et al., 2017). The reanalysis and CCMI simulations are compared to provide confidence in the results obtained from CCMI models.

We use the lowermost stratosphere mass budget approach with a dynamic upper isentropic surface that is determined by fitting to the tropical lapse-rate tropopause as the upper boundary of the lowermost stratosphere (Wang et al., 2022). Herein an upward flux has a positive sign. See Appendix A for a description of this so-called dynamic upper isentrope method in more detail. The derived global air mass fluxes at the upper isentrope may not be zero. Following Olaguer et al. (1992) and Rosenlof (1995), we adjust the diabatic heating rate at the fitted upper isentrope by subtracting or adding a constant to produce a global zero net air mass flux for each month. The multi-model mean (MMM) adjustment is about -0.05 K Day^{-1} (Olaguer et al., 1992), which has little time dependence. We find that similar results are obtained with or without adjustment (not shown). Hereafter, 'diabatic heating' refers to diabatic heating after adjustment, unless otherwise indicated.

The tropopause net air mass and ozone fluxes are the differences of two opposing one-way fluxes (i.e., stratosphere-to-troposphere and troposphere-to-stratosphere transports). In this study, the stratosphere-troposphere exchange is referred to as the net fluxes across tropopause. Following Meul et al. (2018), we divide 1960–2099 into 1960–2000 and 2000–2099 because the atmospheric ODS concentrations peak around 2000. The trends for these two periods are calculated using least-squares fitting. The latitudes with a zero diabatic heating at the fitted isentropic surface are defined as the tropics/extratropics boundaries (Appendix A). The climatological values for 1980–2020 averaged over NH extratropics, SH extratropics, tropics, extratropics, and globe are obtained for each CCMI model, the MMM, and reanalyses. Unless otherwise indicated, the trends in units of % decade^{-1} for 1960–2000 and 2000–2099 are the trends over these periods for each model and the MMM divided by the corresponding climatological values for 1980–2020. Note that using the climatological values over a different period may somewhat impact the magnitudes of the trends in units of % decade^{-1}. Herein a positive (negative) trend in units of % decade^{-1} always indicates an increase (decrease) in magnitudes, regardless of the signs of the variables considered.

3. STE Changes

Before presenting STE results, we show in Figure 1 the time series of the annual-mean tropical-mean lapse-rate tropopause pressure (Figure 1a), temperature (Figure 1e), and fitted upper isentrope (Figure 1i), their climatological values averaged over 1980–2020 (Figures 1b, 1f, and 1j), and their trends for 1960–2000 (Figures 1c, 1g, and 1k) and 2000–2099 (Figures 1d, 1h, and 1l). The tropical tropopause pressure (temperature) climatology from 10 CCMI models ranges from 94 to 112 hPa (190–200 K), and the fitted isentrope ranges from 367 to 382 K. The CCMI MMM of the tropical tropopause pressure (106 hPa), temperature (196 K), and fitted upper isentrope (374 K) climatology agrees well with the ERA5 and MERRA2 reanalyses (Figures 1b, 1f, and 1j). All models simulate a decreasing tropopause pressure (i.e., an increasing tropopause height) from 1960 to 2099 (Figure 1a), consistent with previous studies (e.g., Lin et al., 2017; Lorenz & DeWeaver, 2007; Santer et al., 2003). On the other hand, all models show an increasing tropopause temperature for 1960–2099, except

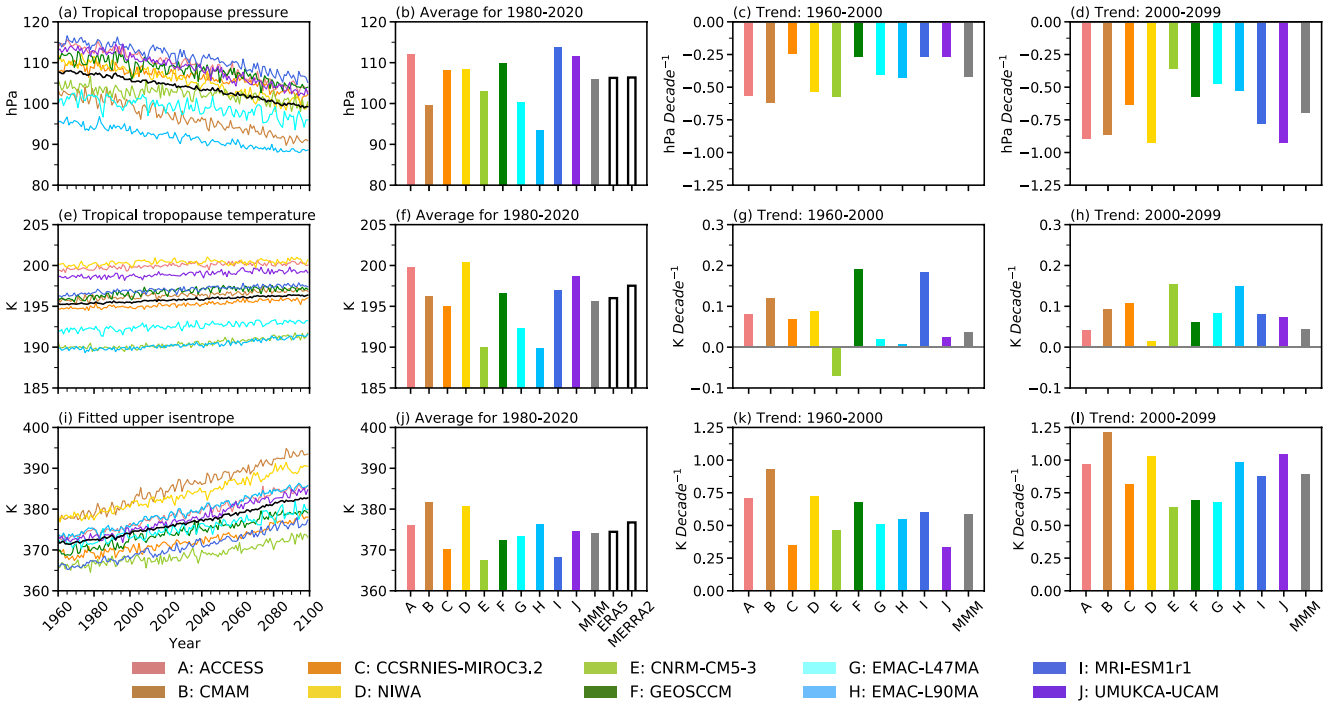

Figure 1. (a) Time series of the annual-mean tropical-mean lapse-rate tropopause pressure (hPa) from 1960 to 2099, (b) its climatological values averaged over 1980–2020, (c) its trends for 1960–2000, and (d) trends for 2000–2099. (e–h), and (i–l) are the same as (a–d) but for tropopause temperature and fitted upper isentrope, respectively. Each color represents one model. The black lines in the first column from the left and gray bars in the second to fourth columns are the multi-model mean (MMM) results. In the second column from the left, the ERA5 and MERRA2 results are shown as white bars with black edges for a comparison.

CNRM-CM5-3 for 1960–2000 (Figure 1g). The magnitude of the MMM tropical tropopause pressure trend over 2000–2099 (−0.7 hPa decade^{-1}) is larger than that over 1960–2000 (−0.4 hPa decade^{-1}) (Figure 1d vs. Figure 1c), while the MMM tropical tropopause temperature trends over 1960–2000 and 2000–2099 are the same (i.e., 0.04 K decade^{-1}) (Figures 1g and 1h). In line with the lower tropopause pressures and higher tropopause temperatures, the fitted upper isentropes are increased consistently from 1960 to 2099 (Figure 1i). The MMM trend of fitted upper isentrope over 2000–2099 (i.e., 0.9 K decade^{-1}) is larger than over 1960–2000 (0.6 K decade^{-1}) (Figure 1l vs. Figure 1k), due to the larger magnitudes of tropical tropopause pressure trends over 2000–2099 than 1960–2000 (Figure 1d vs. Figure 1c). The upper isentropes in CCMI are increased from ∼365 to 378 K in 1960 to 373–394 K in 2099 (Figure 1i), while the tropical tropopause pressures are decreased from ∼95 to 115 to 88–105 hPa (Figure 1a). Therefore, it could be problematic to use a constant upper boundary (e.g., 380 K or 100 hPa) for the lowermost stratosphere in changing climates.

3.1. STE of Air Mass

The annual-mean tropopause net air mass fluxes are shown in Figure 2. The magnitudes of these fluxes averaged over 1980–2020 in CCMI models are 9–12, 7–10, and 17–22 × 10^9 kg s^{-1} in the NH extratropics, SH extratropics, and tropics, respectively, which are close to the corresponding ERA5 and MERRA2 flux magnitudes of 10.8–12.0, 10.2–10.6, and 21.0–22.6 × 10^9 kg s^{-1}, and consistent with previous estimates (e.g., Appenzeller et al., 1996; Schoeberl, 2004; Wang & Fu, 2021). The small differences in the net air mass fluxes from the same reanalyses between this study and Wang and Fu (2021) are because Wang and Fu (2021) used a 380 isentrope that is above those fitted to the reanalysis tropical tropopause (Figure 1j). The air mass flux magnitudes over the NH extratropics are larger than the SH extratropics counterparts, in line with past studies (e.g., Gettelman et al., 1997; Olsen et al., 2004; Yang et al., 2016). The magnitudes of MMM air mass STEs, that is, 9.9, 8.2, and 18.2 × 10^9 kg s^{-1} in the NH extratropics, SH extratropics, and tropics, respectively, are all somewhat smaller than those from reanalyses (Figures 2b, 2f, and 2j).

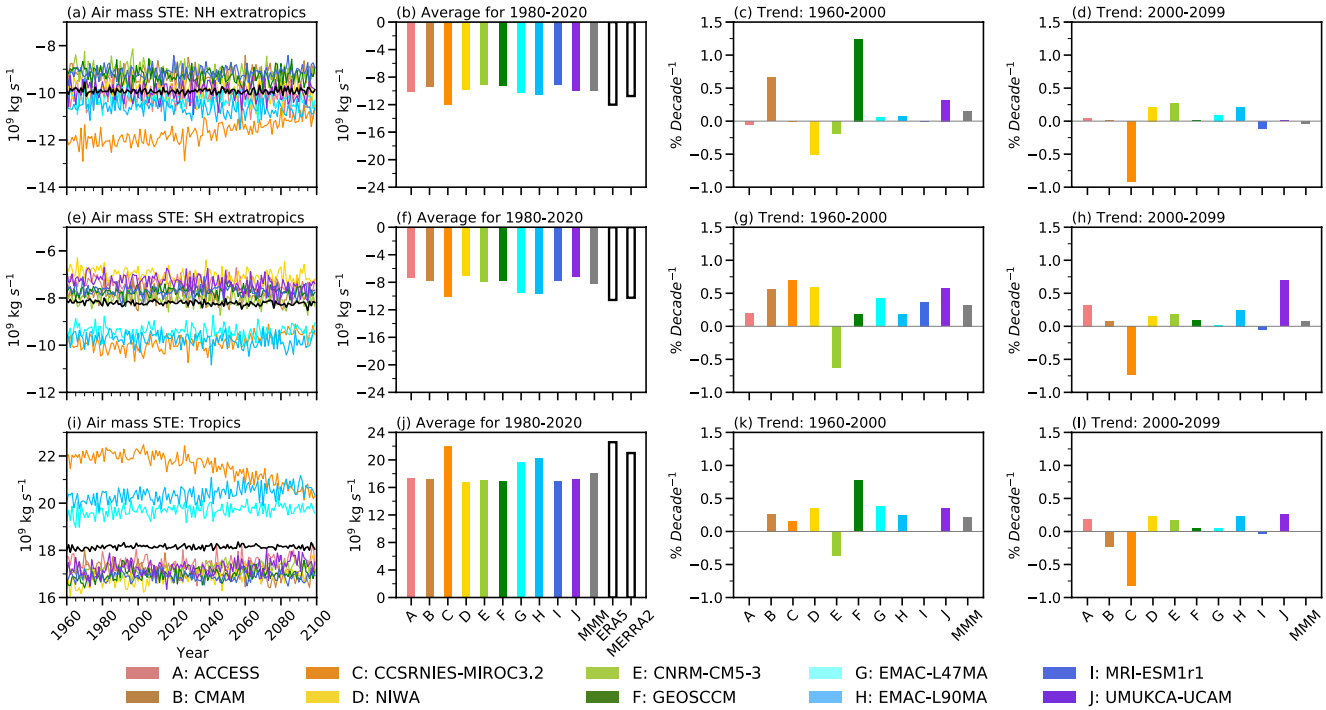

Figure 2. The same as Figure 1, but for annual-mean tropopause net air mass fluxes (10^9 kg s^{-1}), that is, air mass stratosphere-troposphere exchange (STE), over the (a–d) Northern Hemisphere extratropics, (e–h) Southern Hemisphere extratropics, and (i–l) tropics. The trends' units are in % $decade^{-1}$, which are the mass flux trends scaled by the corresponding climatological values over 1980–2020.

In the NH extratropics, the signs of air mass STE trends from various CCMI models for 1960–2000 can be either positive or negative, and the MMM trend is 0.15% $decade^{-1}$ (Figure 2c). In the SH extratropics and the tropics for 1960–2000, all models except CNRM-CM5-3 show increased magnitudes of air mass STEs, with MMM trends of 0.3% and 0.2% $decade^{-1}$, respectively (Figures 2g and 2k). For 2000–2099, the magnitudes of MMM air mass STE trends in the NH extratropics, SH extratropics, and tropics are all close to zero (i.e., −0.04%, 0.08%, and −0.01% $decade^{-1}$, respectively) (Figures 2d, 2h, and 2l). As will be shown in Section 4, the small changes in air mass STEs for both 1960–2000 and 2000–2099 are due to the cancellation between changes in diabatic heating and isentropic density. Such a result is consistent with Oberländer-Hayn et al. (2016) who showed that the residual mass transport between the troposphere and stratosphere due to global warming changes little after considering changes in tropopause heights. Note that the small increases in air mass STEs for 1960–2000 could be partly because part of the BDC strengthening is driven by ozone depletion (Fu et al., 2015, 2019; Lin & Fu, 2013), which has a negligible impact on the tropopause height. For 2000–2099, in response to ozone recovery, the BDC is weakening (Lin & Fu, 2013) with a rate of ∼40% of that for 1960–2000, which might also play a role in modulating the air mass STE trend for 2000–2099.

3.2. STE of Ozone

The annual-mean tropopause net ozone fluxes are shown in Figure 3, with annual and seasonal mean values for both climatology and trends provided in Table 1. Averaged over 1980–2020, the CCMI annual-mean tropopause net ozone flux magnitudes in the NH extratropics, SH extratropics, tropics, extratropics, and globe are 207–338, 114–259, 50–185, 321–592, and 217–447 Tg $year^{-1}$, respectively, with corresponding MMM magnitudes of 282, 196, 138, 478, 340 Tg $year^{-1}$ (Figure 3 and Table 1). The large range in the ozone STEs from various models indicates the importance of analyzing multiple model simulations. The MMM magnitudes are close to the estimates based on the ERA5 and MERRA2 of 306–343, 225–241, 169–202, 531–583, and 363–382 Tg $year^{-1}$ in the NH extratropics, SH extratropics, tropics, extratropics, and globe, respectively, and are also consistent with previous studies (e.g., Gettelman et al., 1997; Hsu et al., 2005; Olsen et al., 2013; Wang & Fu, 2021; Yang et al., 2016). The magnitudes of ozone STEs in the NH extratropics maximize in the spring (Table 1) because of the seasonal breathing of the lowermost stratosphere ozone mass (Appenzeller et al., 1996). In the SH extra-

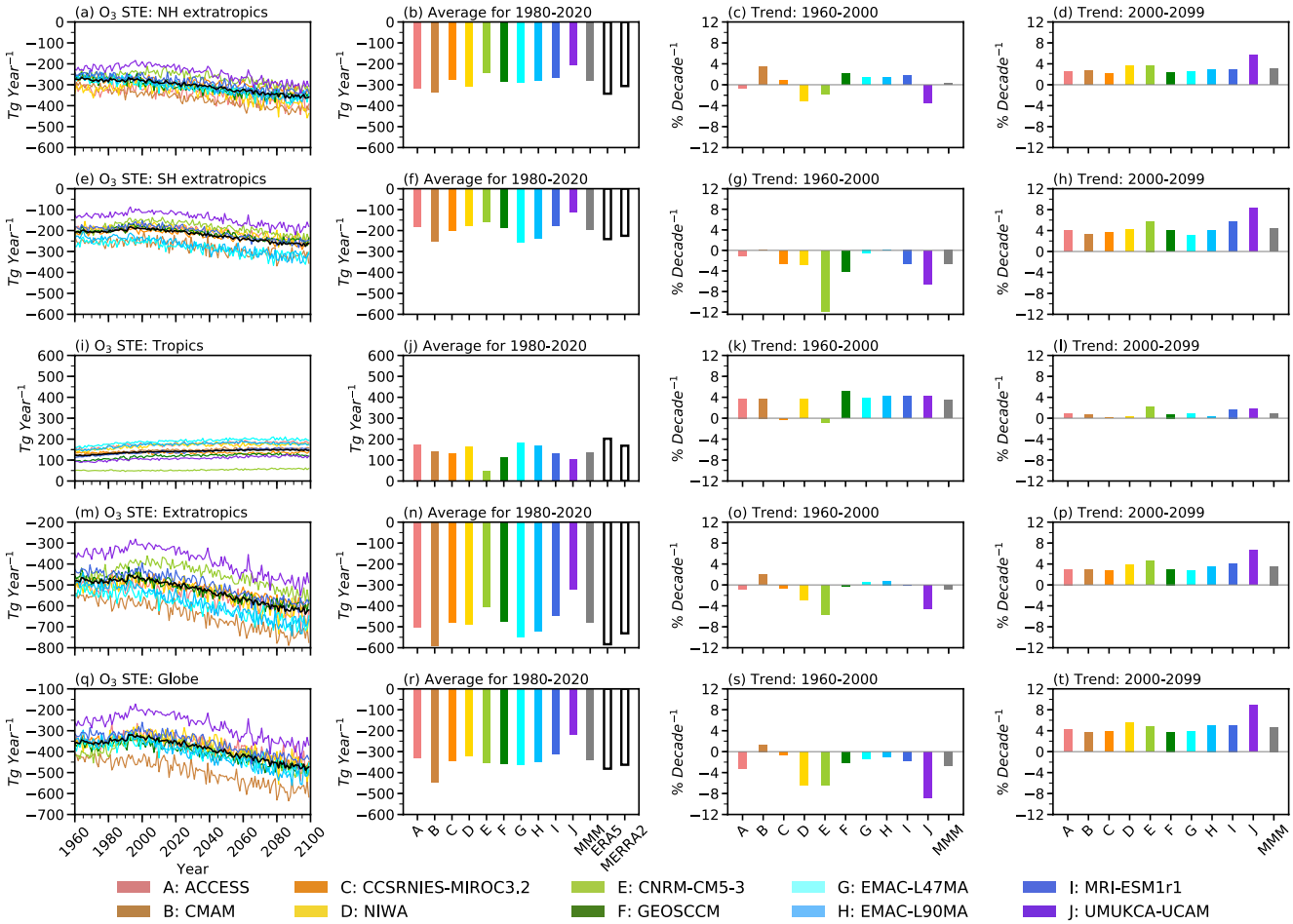

Figure 3. The same as Figure 1, but for annual-mean tropopause net ozone fluxes (Tg year^{-1}), that is, ozone stratosphere-troposphere exchange (STE), over (a–d) the Northern Hemisphere extratropics, (e–h) Southern Hemisphere extratropics, (i–l) tropics, (m–p) extratropics, and (q–t) globe. The trends' units are in % decade^{-1}, which are the ozone flux trends scaled by the corresponding climatological values over 1980–2020.

tropics, the ozone STE magnitude in spring is smaller than in winter (Table 1) because of the ODS-induced ozone depletion during spring. The upward ozone fluxes in the tropics compensate for about 12%–34% of the extratropical downward ozone fluxes, with a MMM value of 29%. The MMM annual mean ozone STE climatology magnitude is 478 Tg year^{-1} over the extratropics and 340 Tg year^{-1} over the globe (Table 1). Therefore, the tropical upward ozone flux should not be neglected for the global ozone STE (Wang & Fu, 2021).

Table 1
Annual and Seasonal Mean Tropopause Net Ozone Flux Climatology (Tg year^{-1}), That Is, Ozone Stratosphere-Troposphere Exchange (STE), Averaged Over 1980–2020, in the Northern Hemisphere (NH) Extratropics, Southern Hemisphere (SH) Extratropics, Tropics, Extratropics, and Globe

	NH extratropics		SH extratropics		Tropics		Extratropics		Globe	
	Tg year^{-1} (% decade^{-1} for 1960–2000, % decade^{-1} for 2000–2099)									
ANN	−282.3	(0.3, **3.0**)	−195.6	**(−2.7, 4.3)**	137.6	**(3.4, 0.8)**	−477.9	**(−0.9, 3.5)**	−340.3	**(−2.7, 4.7)**
DJF	−323.8	**(1.0, 2.6)**	−122.6	**(−12.3, 6.7)**	151.9	**(3.1, 0.7)**	−446.5	**(−2.6, 3−7)**	−294.5	**(−5.6, 5.3)**
MAM	−474.0	(0.5, **3.0**)	−158.1	**(−5.3, 6.9)**	131.2	**(3.3, 0.7)**	−632.1	**(−1.0, 4.0)**	−500.9	**(−2.1, 4.8)**
JJA	−253.2	(0.0, **2.0**)	−270.3	(0.5, **2.7**)	145.4	**(3.1, 1.2)**	−523.5	(0.3, **2.4**)	−378.1	**(−0.8, 2.8)**
SON	−78.0	**(−2.3, 7.9)**	−231.4	(0.5, **3.2**)	121.9	**(4.4, 0.5)**	−309.4	(−0.2, **4.4**)	−187.5	**(−3.2, 6.9)**

Note. The numbers in the parentheses are the corresponding trends (% decade^{-1}) for 1960–2000 and 2000–2099. Trend numbers shown in bold are statistically significant at a 95% confidence level following the Santer et al. (2000) method. The multi-model mean results are shown here.

The MMM annual mean ozone STE trends for 1960–2000 are 0.3%, −2.7%, 3.4%, −0.9%, and −2.7% decade^{-1} over the NH extratropics, SH extratropics, tropics, extratropics, and globe, respectively (Table 1). The decreased MMM annual-mean global ozone STE magnitude for 1960–2000 (i.e., −2.7% decade^{-1}) is caused by both more troposphere-to-stratosphere ozone transport over the tropics (52%) and less stratosphere-to-troposphere ozone transport over the extratropics (48%) from Table 1. As will be shown in Section 5, the decreased ozone STE magnitude in the SH extratropics for 1960–2000 is caused by ODS-induced ozone depletion, while the small change in ozone STE in the NH extratropics is due to a cancellation between GHG/SST and ODS effects. The increased ozone STE over the tropics is due to both increased tropospheric ozone and tropopause height for 1960–2000 (Section 5). For 2000–2099, all CCMI models predict increased magnitudes of annual-mean ozone STEs over the NH extratropics, SH extratropics, tropics, extratropics, and globe, which from various CCMI models have ranges of 2.1–5.7, 3.1–8.2, 0–2.2, 2.7–6.6, 3.7–8.9 with MMM trends of 3.0%, 4.3%, 0.8%, 3.5%, and 4.7% decade^{-1}, respectively (Figure 3 and Table 1). In December-January-February (DJF), March-April-May (MAM), June-July-August (JJA), and September-October-November (SON), the MMM trends in global ozone STEs are −5.6%, −2.1%, −0.8%, −3.2% decade^{-1} for 1960–2000 and 5.3%, 4.8%, 2.8%, 6.9% decade^{-1} for 2000–2099, respectively (Table 1).

The relative increase in annual-mean ozone STE magnitude for 2000–2099 over the globe (i.e., 4.7% decade^{-1} in Table 1) is more than that over extratropics (i.e., 3.5% decade^{-1} in Table 1). This is mainly because the ozone STE over extratropics has a larger climatology magnitude, that is, a larger denominator, than that over the globe. For 1960–2000, a larger relative decrease in annual-mean ozone STE magnitude over the globe than that over the extratropics (i.e., −2.7 vs. −0.9% decade^{-1} in Table 1) is also due to a significantly increased ozone upward flux over the tropics during this period.

The importance of using dynamic isentropes to estimate STEs of air mass (Table A1) and ozone (Table A2) is shown and discussed in Appendix B by comparing the results with those using a fixed isentrope. For example, using a fixed isentrope of 380 K with 2 potential vorticity unit (PVU) for extratropical tropopause following Appenzeller et al. (1996), the MMM annual-mean ozone STE trend over extratropics for 2000–2099 becomes 4.4% decade^{-1} versus 3.5% decade^{-1} using the dynamic isentropes. On the other hand, using a fixed isentrope of 380 K along with the WMO tropopause for both tropics and extratropics following Wang and Fu (2021), the MMM annual-mean ozone STE trend over extratropics for 2000–2099 is 2.5% decade^{-1}. We also notice large differences in estimated ozone STEs over the tropics by using fixed versus dynamic isentropes (Table A2). Wang et al. (2022) discussed the biases in estimated air mass STE climatologies and changes due to the use of a fixed isentrope in detail, which can also be seen in Table A1.

4. Causes for the STE Changes

The annual mean tropopause net air mass and ozone fluxes and changes can be well approximated by the diabatic fluxes and changes across the upper isentropic surfaces (Olsen et al., 2013; Schoeberl, 2004; Wang et al., 2022; Wang & Fu, 2021) (also see Appendix A). The diabatic fluxes are determined by diabatic heating, isentropic density, tropical boundaries, and ozone concentrations at the fitted isentropic surface (Appendix A). In this section, we first present the changes in diabatic heating, isentropic density, tropical boundaries, and ozone concentrations, and then examine their roles in determining the changes of air mass and ozone fluxes across the upper isentropic surface for both 1960–2000 and 2000–2099.

4.1. Changes in Diabatic Heating, Isentropic Density, Tropical Boundaries, and Ozone Concentration

Figure 4 shows the time series of annual-mean adjusted diabatic heating rates at the fitted upper isentrope averaged over the NH extratropics, SH extratropics, and tropics (Figures 4a, 4e, and 4i), with the corresponding climatological values for 1980–2020 (Figures 4b, 4f, and 4j), and trends for 1960–2000 (Figures 4c, 4g, and 4k) and 2000–2099 (Figures 4d, 4h, and 4l). The diabatic heating is negative in the extratropics and positive in the tropics. The CCMI MMM magnitudes of climatological values in the SH extratropics and tropics are close to ERA5 and MERRA2 estimates (Figures 4f and 4j), but are somewhat smaller than the reanalyses in the NH extratropics (Figure 4b). Except for the CCSRNIES-MIROC3.2 in the tropics for 2000–2099 (Figure 4l), all models predict increased magnitudes of annual-mean diabatic heating in all regions. The MMM trends for 1960–2000 (2000–2099) in the NH extratropics, SH extratropics, and tropics are 0.66 (0.69), 0.70 (0.63), and 0.64

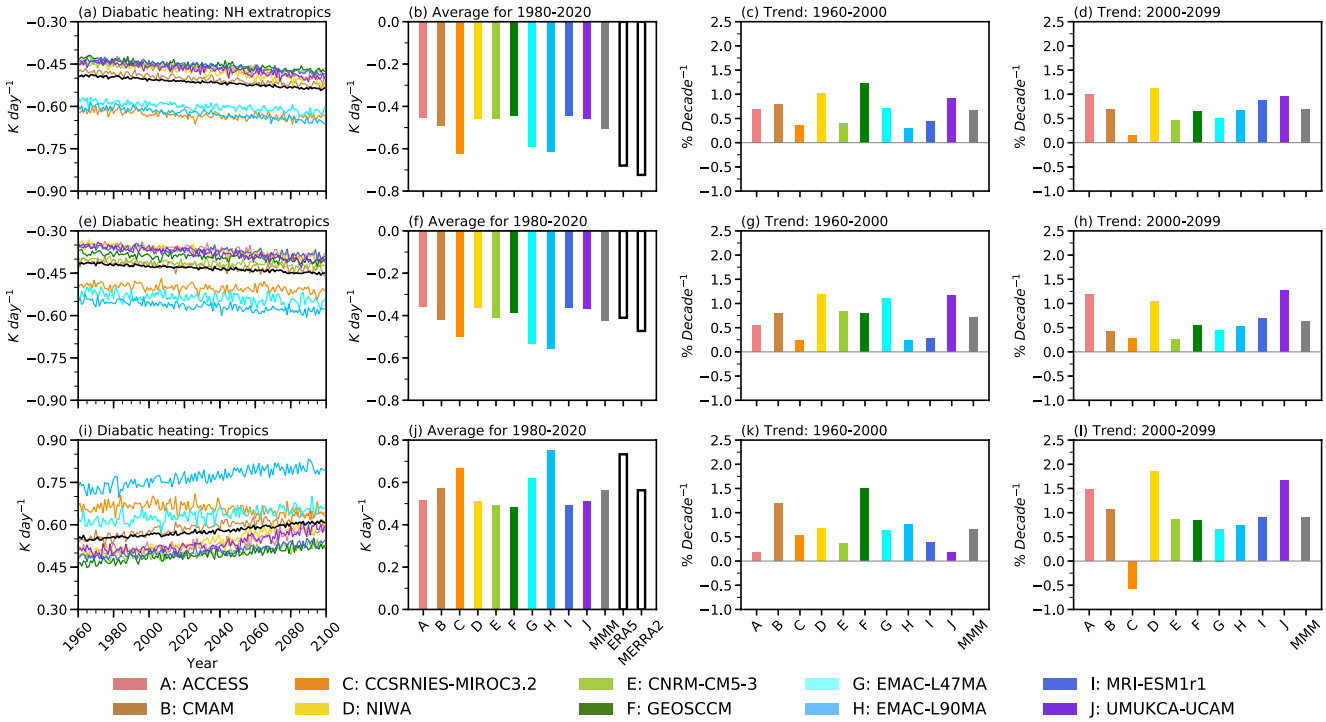

Figure 4. The same as Figure 1, but for the annual-mean adjusted diabatic heating rates (K day^{-1}) at the fitted upper isentrope averaged over the (a–d) Northern Hemisphere extratropics, (e–h) Southern Hemisphere extratropics, and (i–l) tropics. The trends' units are in % decade^{-1}, which are the diabatic heating rate trends scaled by the corresponding climatological values over 1980–2020.

(0.89) % decade^{-1}, respectively. The stronger diabatic heating in the tropics (Figures 4k and 4l) but stronger diabatic cooling in the extratropics (Figures 4c, 4d, 4g, and 4h) for 1960–2000 and 2000–2099 in the CCMI models are generally consistent with previous studies that show a strengthening BDC in a warming world (e.g., Abalos et al., 2021; Butchart, 2014; Butchart et al., 2006; Li et al., 2008; Lin & Fu, 2013). The diabatic heating at the upper isentropic surface is contributed by longwave and shortwave radiative heatings (Figures S1 and S2 in Supporting Information S1), which are discussed in Appendix C.

Figure 5 shows the results for isentropic density. There are good agreements between CCMI models and reanalysis (Figures 5b, 5f, and 5j). All CCMI models show decreased isentropic density at the fitted upper isentrope in all regions for both 1960–2000 and 2000–2099, which are largely related to the higher upper isentropic surfaces, corresponding to the higher tropical tropopause heights in a warming world (Figure 1).

The results of the tropical boundary (i.e., latitudes with zero diabatic heating at the fitted upper isentrope) in the NH, SH, and the tropical width are shown in Figure 6. The CCMI climatological results agree well with the reanalyses (Figures 6b, 6f, and 6j). For 1960–2000, the trends of the SH tropical boundary and tropical width are inconclusive, although the NH tropical boundary indicates a poleward shift (Figures 6c, 6g, and 6k). On the other hand, all CCMI models simulate equatorward shifts of the tropical boundary in both NH and SH and a narrowing tropical width for 2000–2099 (Figures 6d, 6h, and 6l). Such a result is in line with Li et al. (2010) and Hardiman et al. (2014), who showed the narrowing of the upwelling branch of the BDC due to climate change using chemistry-climate model simulations. The trends of the NH and SH tropical boundaries and tropical width for 2000–2099 are −0.09, −0.08, and −0.17 latitude degree decade^{-1}, respectively.

The results of ozone concentrations at the fitted upper isentrope are presented in Figure 7. The CCMI climatological values are in good agreement with ERA5 and MERRA2 over the SH extratropics and tropics (Figures 7f and 7j), but somewhat smaller than the reanalyses over the NH extratropics (Figure 7b). For 1960–2000, the trends of mean ozone concentrations in the NH extratropics range from −3.7% to 2.8% decade^{-1}, with a MMM trend of −0.02% decade^{-1} (Figure 7c). This is due to the opposite effects of GHG/SST and ODS (Section 5). In the SH extratropics, all models show decreases in ozone concentrations for 1960–2000 (ranging from −0.11% to −18.3% decade^{-1}), with a MMM trend of −4.6% decade^{-1} (Figure 7g), which is caused by large ozone depletion due to

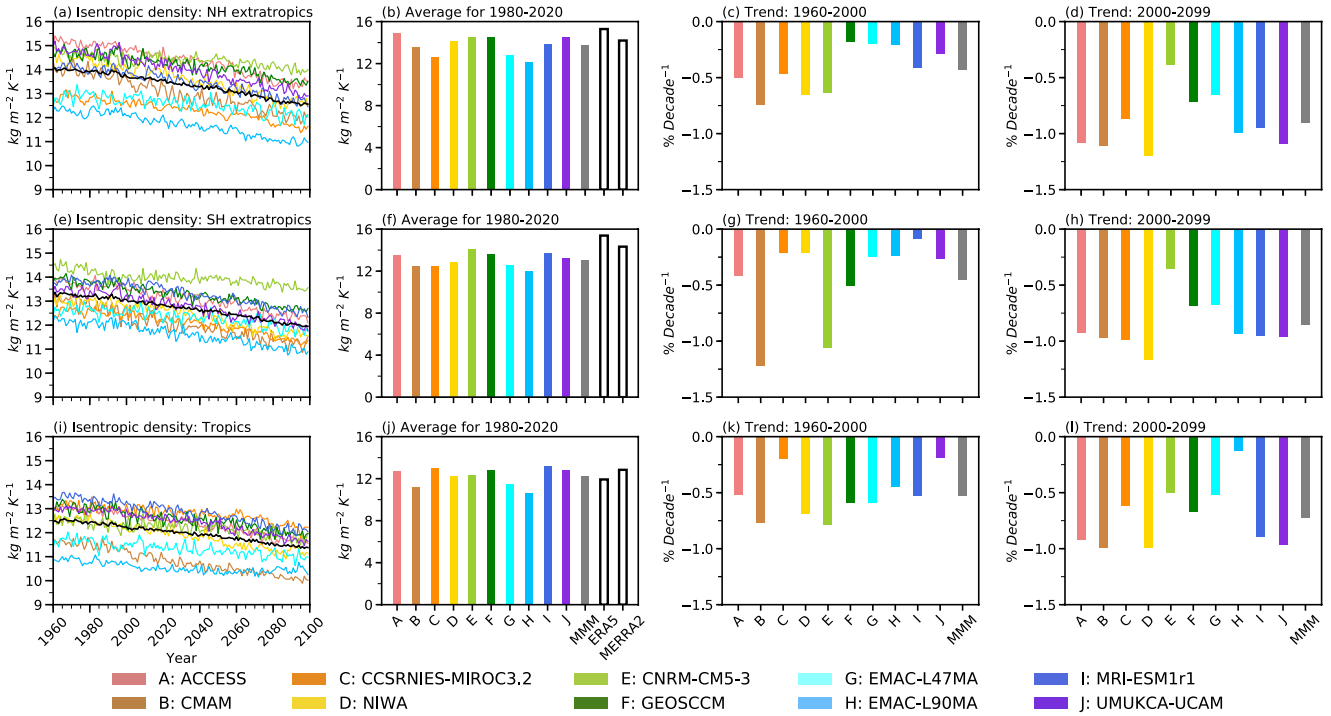

Figure 5. The same as Figure 1, but for the annual-mean isentropic density (kg m^{-2} K^{-1}) at the fitted upper isentrope averaged over the (a–d) Northern Hemisphere extratropics, (e–h) Southern Hemisphere extratropics, and (i–l) tropics. The trends' units are in % $decade^{-1}$, which are the isentropic density trends scaled by the corresponding climatological values over 1980–2020.

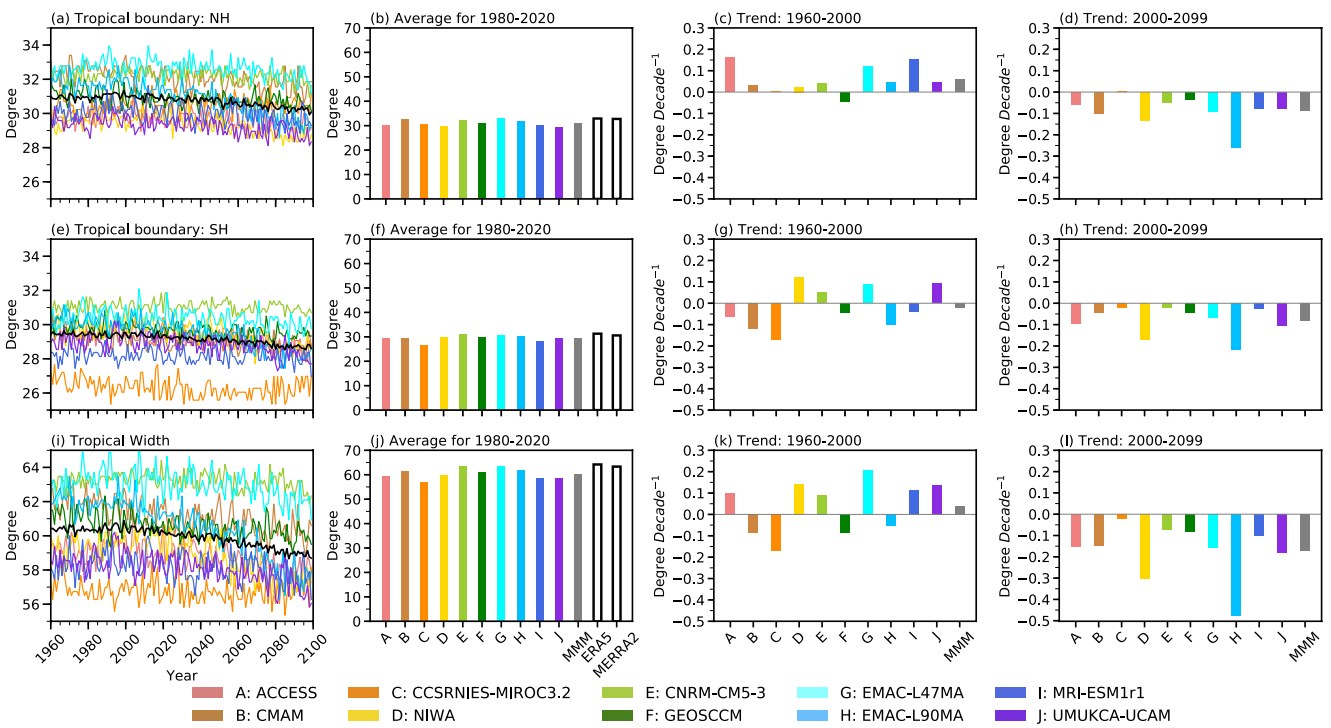

Figure 6. The same as Figure 1, but for the annual-mean tropical boundary (i.e., latitudes with zero diabatic heating at the fitted upper isentrope) in the (a–d) Northern Hemisphere, and (e–h) Southern Hemisphere, and for (i–l) the annual-mean tropical width.

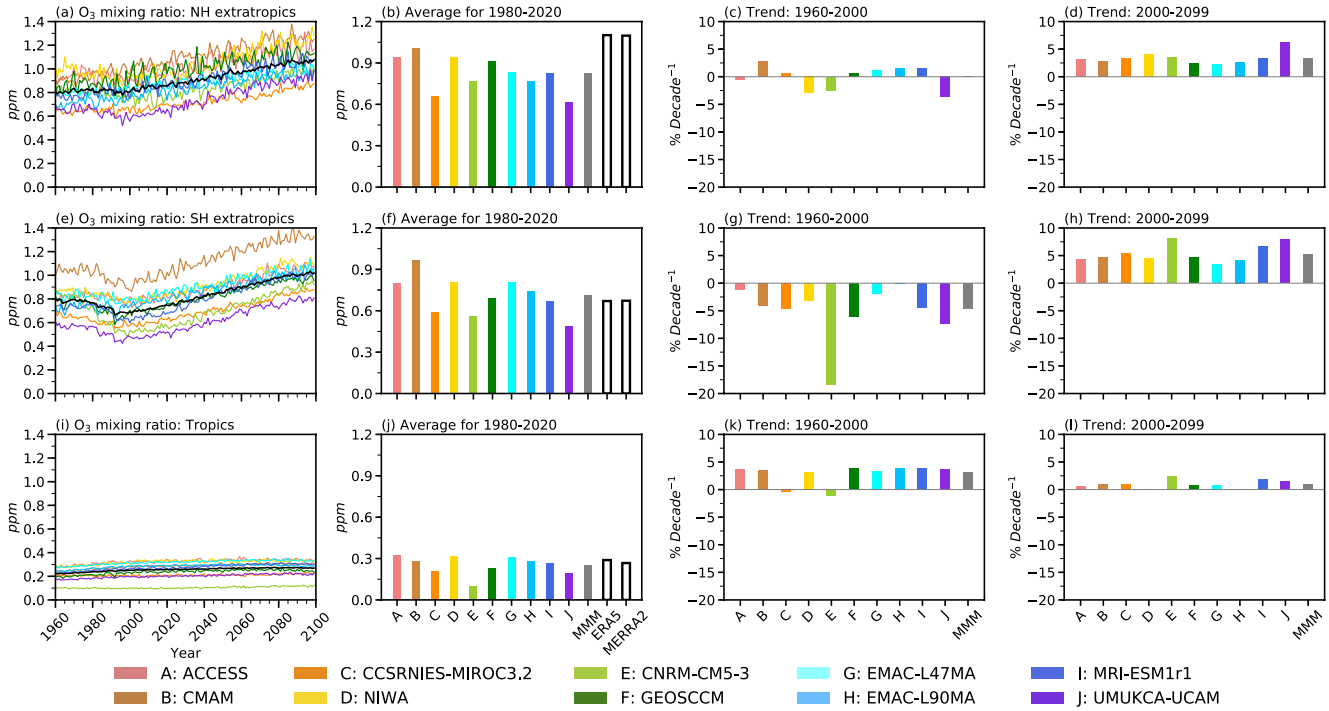

Figure 7. The same as Figure 1, but for annual-mean ozone mass mixing ratio (ppm) at the fitted upper isentrope averaged over the (a–d) Northern Hemisphere extratropics, (e–h) Southern Hemisphere extratropics, and (i–l) tropics. The trends' units are in % decade^{-1}, which are the ozone mass mixing ratio trends scaled by the corresponding climatological values over 1980–2020.

ODS (Solomon et al., 2017). On the other hand, all models (except CCSRNIES-MIROC3.2 and CNRM-CM5-3) show increased ozone concentrations at the fitted upper isentrope in the tropics for 1960–2000 (Figure 7k). For 2000–2099, all models predict increased ozone concentrations at the fitted upper isentrope in all regions, with MMM trends of 3.3%, 5.1%, and 0.9% decade^{-1} in the NH extratropics, SH extratropics, and tropics, respectively (Figures 7d, 7h, and 7l). The MMM ozone trend in the tropics for 2000–2099 is much smaller than its counterpart for 1960–2099, which may be related to the reduced ozone precursor emissions due to the action of tropospheric ozone control (e.g., Cooper et al., 2014). The smaller ozone increases in the tropics for 2000–2099 versus 1960–2000 could also explain the smaller tropical ozone STE trends for 2000–2099 versus 1960–2000 (Figure 3l vs. Figure 3k).

4.2. Attribution of Ozone STE Changes to Individual Components

We further quantify the individual contributions from changes in tropical boundaries, diabatic heating, isentropic density, and ozone concentrations to changes in air mass and ozone STEs (Wang et al., 2022; Wang & Fu, 2021) for both periods. First, we calculate the monthly climatology fields of diabatic heating, isentropic density, tropical boundary, and ozone concentrations for each model for 1960–2000. Second, we replace the monthly climatology field of the tropical boundary with the monthly tropical boundary time series for 1960–2000, but retain the monthly climatology fields of diabatic heating, isentropic density, and ozone concentrations. Then, we replace the monthly climatology field of isentropic density with the monthly isentropic density time series for 1960–2000, but retain the monthly climatology fields of diabatic heating and ozone. We continue replacing the monthly climatology field of diabatic heating with the 1960–2000 time series and again retain the monthly ozone climatology field. Finally, we replace the monthly ozone climatology field with the 1960–2000 ozone time series (i.e., all monthly fields for 1960–2000). The monthly air mass and ozone STEs and their trends are calculated for each case, and the trend differences between the two cases are referred to as the individual contribution from the field replaced (the first case has a zero trend). The same calculations for 2000–2099 are performed. The replacement order has a negligible impact on the results (not shown), which indicates that the contribution from the nonlinear term is small despite that these variables might not be independent of each other.

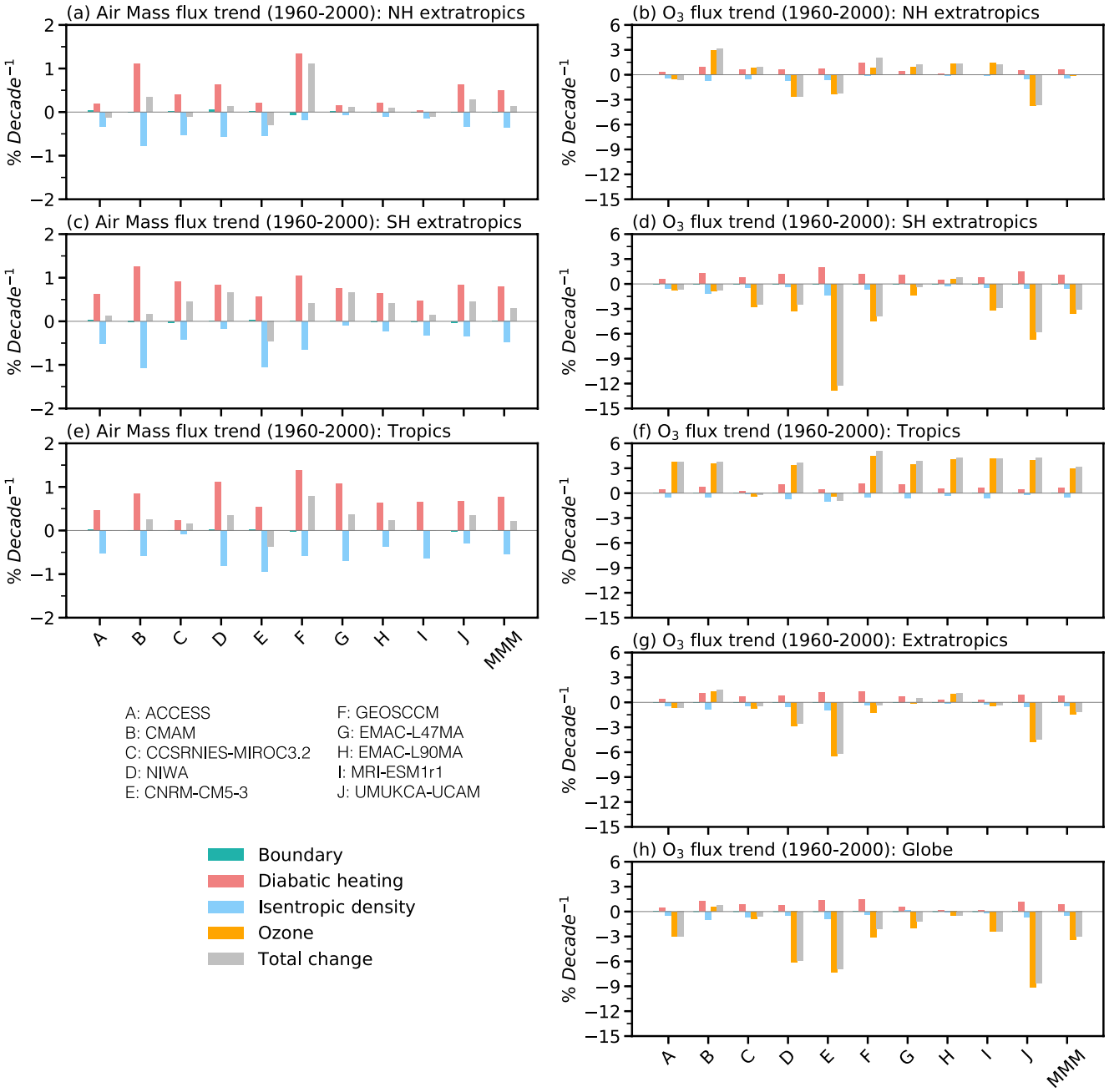

Figure 8. The trends of diabatic air mass (left) and ozone fluxes (right) across the fitted upper isentrope for 1960–2000 (gray) and trends due to the changes in tropics/extratropics boundaries (green), diabatic heating (pink), isentropic density (blue), and ozone concentrations (orange) for the individual model and the multi-model mean (MMM). See the legend for the name of each model.

The results for 1960–2000 and 2000–2099 are shown in Figures 8 and 9, respectively. The increased magnitudes of diabatic heating (Figure 4) increase air mass STE magnitudes, while decreased isentropic density (Figure 5) decreases them (left columns in Figures 8 and 9). The opposite change signs in diabatic heating and isentropic density suggest a close coupling of these two variables in the lower stratosphere. The two competing effects result in small changes in air mass STEs, although there are a few exceptions, such as CCSRNIES-MIROC3.2 for 2000–2099. The contributions from tropical boundary changes (Figure 6) to air mass and ozone STEs are small in all regions from all models. On the other hand, the changes in ozone STEs in all regions are dominated by changes in ozone concentrations (right columns in Figures 8 and 9). Those results are consistent with Wang

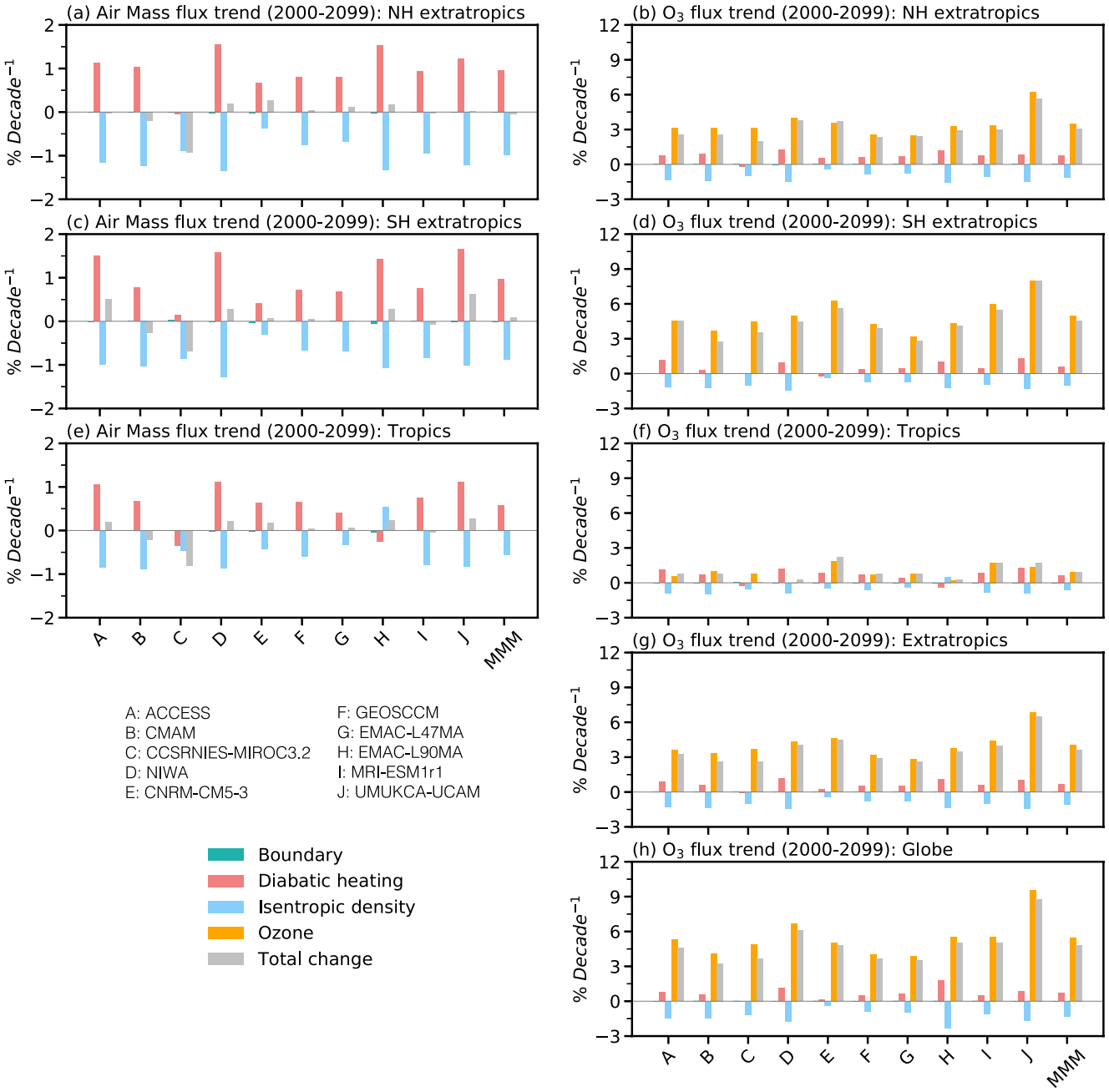

Figure 9. The same as Figure 8 but for trends between 2000 and 2099.

et al. (2022), who used the WACCM6 simulations and showed that decreased ozone STEs in LGM versus the Preindustrial time are mainly caused by decreased ozone in the extratropical lower stratosphere.

5. GHG/SST and ODS Contributions

In this section, the contributions of GHG/SST and ODS to ozone STEs changes are quantified. We use four models including ACCESS, CMAM, CCSRNIES-MIROC3.2, and NIWA which have both SEN-C2-fGHG and SEN-C2-fODS experiments (Table S1 in Supporting Information S1). The MMM in this subsection is thus the mean of these four models. The impact of GHG/SST on the ozone STEs, which is also referred to as climate-induced impact/change in this study, can be through the BDC changes (e.g., Brasseur & Solomon, 2006; Butchart, 2014;

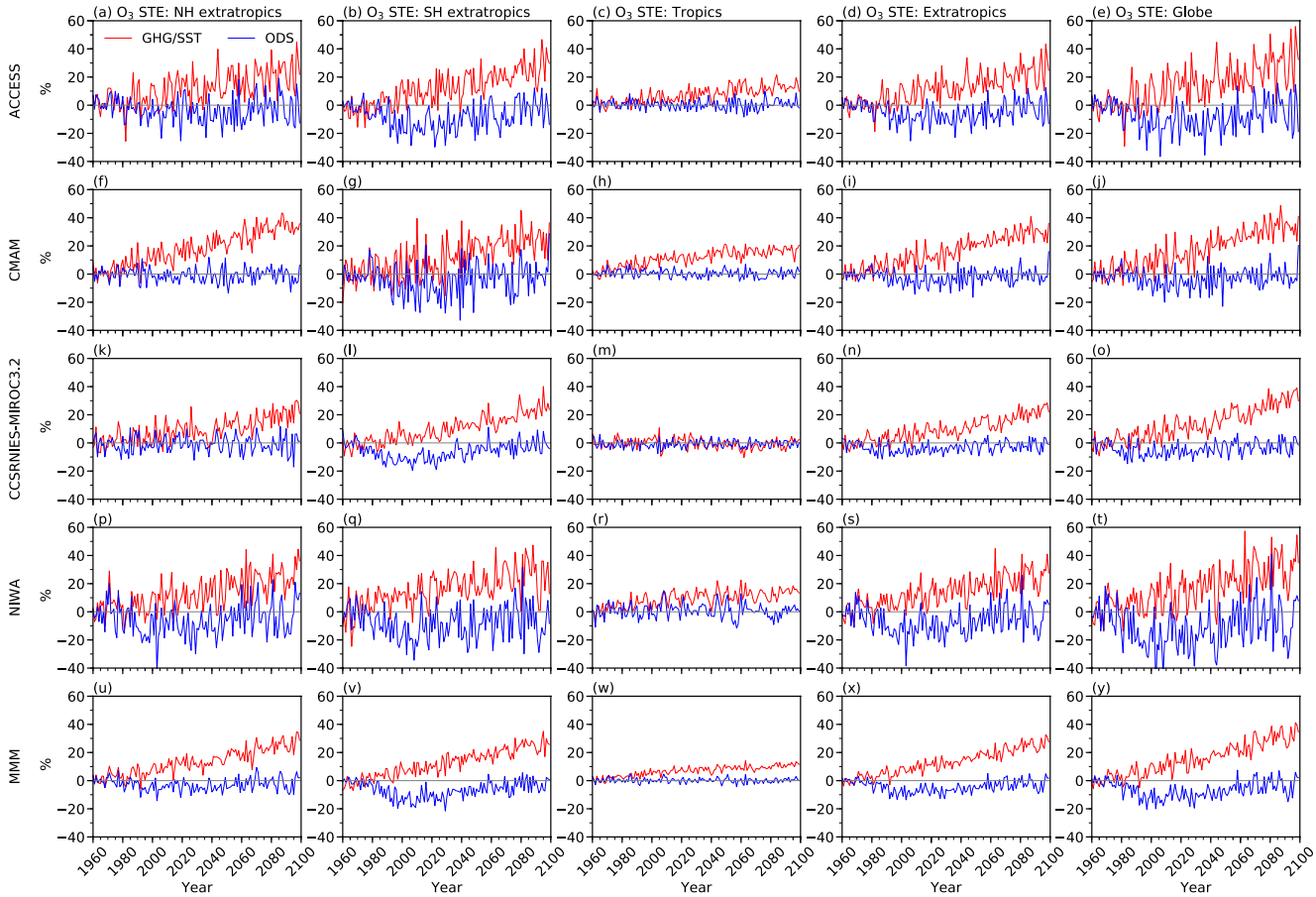

Figure 10. Time series of annual-mean tropopause net ozone fluxes, that is, ozone stratosphere-troposphere exchange (STE), due to the changes in greenhouse gases and sea surface temperatures (GHG/SST, red) and ozone-depleting substances (ODS, blue) between 1960 and 2099 in the Northern Hemisphere extratropics (the first column), Southern Hemisphere extratropics (the second column), tropics (the third column), extratropics (the fourth column), and the globe (the fifth column) for (a–e) ACCESS, (f–j) CMAM, (k–o) CCSRNIES-MIROC3.2, (p–t) NIWA, and (u–y) the multi-model mean (MMM) of the four models. The time series of changes due to GHG/SST (ODS) over 1960–2099 are the differences between REF-C2 and SEN-C2-fGHG (SEN-C2-fODS), scaled by the REF-C2 climatological values over 1980–2020.

Li et al., 2009; Wang et al., 2020). And stratospheric chemistry related to ozone temperature-dependent reactions (e.g., Match & Gerber, 2022). In addition, the ozone mixing ratio at the fitted isentropic surface would increase as the tropical tropopause becomes higher in a warming world for given ozone fields since ozone mixing ratio increases with height in the tropical upper troposphere and lower stratosphere and in the extratropical lower stratosphere. For the ODS impact on ozone STEs, in addition to the ozone depletion caused by ODS (e.g., Solomon, 1999), the ODS would also lead to changes in BDC (e.g., Abalos et al., 2019; Li et al., 2008; Lin & Fu, 2013; Polvani et al., 2019). In this study, the ODS impacts on ozone STEs include both chemical depletion and BDC change effects, but the chemical depletion effect dominates.

Figure 10 shows the time series of changes in tropopause net ozone fluxes due to GHG/SST and ODS changes for 1960–2099 over various regions from various models and MMM. The corresponding time series for ozone mass mixing ratio at the fitted upper isentrope are shown in Figure S3 in Supporting Information S1. Note that the GHG/SST (ODS) effects are the differences between REF-C2 and SEN-C2-fGHG (SEN-C2-fODS), scaled by the corresponding REF-C2 climatology over 1980–2020. Since ozone STE changes are largely determined by the ozone concentration changes, the time series in Figure 10 over NH extratropics, SH extratropics, and tropics are very similar to the corresponding ozone mixing ratio difference time series in Figure S3 in Supporting Information S1. Due to ODS effects, the magnitude decreases in ozone concentrations and ozone STEs in the SH extratropics peak around 2000, then gradually recover by 2080. In the NH extratropics, the ozone changes due to the ODS are relatively small, especially in CMAM and CCSRNIES-MIROC3.2. In ACCESS and NIWA,

the magnitudes of ozone concentration and ozone STEs show modest initial decreases due to ODS, peak around 2000, and then gradually recover by 2060, which is a bit earlier compared to the SH extratropics. Over the tropics, the impacts of ODS on ozone concentrations and ozone STEs are small. On the other hand, GHG/SST effects lead to increases in ozone concentrations and ozone STEs from all models over all regions for both periods of 1960–2000 and 2000–2099.

The trends of tropopause net ozone fluxes and the trends due to GHG/SST, ODS, and other changes for 1960–2000 and 2000–2099 are shown in Figure 11. The "other" change here is the difference between the trend in REF-C2 and the summation of trends due to GHG/SST and ODS effects, which is due to the non-SST impacts of volcanic eruptions, solar cycle, and tropospheric ozone changes. The trends are in units of % decade^{-1}, scaled by REF-C2 climatology averaged over 1980–2020. For 1960–2000, GHG/SST leads to increased ozone STE magnitudes over all regions (left column of Figure 11). ODS leads to decreased magnitudes over NH extratropics (Figure 11a) and especially over SH extratropics (Figure 11c), but not over tropics (Figure 11e). The "other" effect increases ozone STE over the tropics (Figure 11e) while it increases/decreases the STE magnitudes somewhat over the NH/SH extratropics (Figures 11a and 11c), leading to little impact on the extratropics (Figure 11g). For the MMM in the NH extratropics and the extratropics, magnitudes of ODS effects are comparable with GHG/SST effect, leaving small changes in ozone STEs there (Figures 11a and 11g). However, in the SH extratropics and globe, the magnitudes of ODS effects are larger than GHG/SST effects, leading to decreases in ozone STEs (Figures 11c and 11i). In the tropics, the ODS effect for 1960–2000 is close to zero, while GHG/SST and "other" effects are comparable (Figure 11e). The latter is caused by large increases in tropospheric ozone concentrations, due to increased tropospheric ozone precursor emissions for 1960–2000 (see Section 6). A decreased global ozone STE magnitude (Figure 11i) was caused by the ODS effect that is partly compensated by the GHG/SST effect, but is somewhat enhanced by the "other" effect associated with more ozone transport from the tropical troposphere to stratosphere.

For 2000–2099, the ozone STE magnitude increase in the NH extratropics is dominated by the GHG/SST effect (Figure 11b). In the SH extratropics, the ODS effect on ozone STE is comparable but somewhat smaller than the GHG/SST effect (Figure 11d), both increasing the ozone STE magnitude. Both GHG/SST and ODS effects are small in the tropics (Figure 11f). About one-third of the MMM global ozone STE magnitude increase for 2000–2099 is due to ozone recovery caused by the phaseout of ODS, and two-thirds is due to the GHG/SST effect (Figure 11j).

It is noted that the relative trends of ozone STE and ozone mixing ratios at the fitted isentrope in the NH extratropics for 1960–2000 can be either positive or negative among CCMI models (see Figures 3c and 7c). This is because GHG/SST and ODS for 1960–2000 have positive and negative effects, respectively, and their magnitudes can be quite different among the CCMI models (Figure 11a). For instance, the ODS effect is −4.3% decade^{-1} in NIWA but is near zero in CMAM, while the corresponding GHG/SST effect is near zero in NIWA but 2.8% decade^{-1} in CMAM.

Changes in ozone STEs are largely determined by ozone concentration changes (Figures 8 and 9). BDC significantly modulates ozone concentrations in the lower stratosphere (e.g., Brasseur & Solomon, 2006; Li et al., 2009; Wang et al., 2020). The stratospheric temperature also affects the stratospheric ozone through the temperature-dependent Chapman reactions (e.g., Chiodo et al., 2018; Haigh & Pyle, 1982; Jonsson et al., 2004; Match & Gerber, 2022). On the other hand, the ozone concentration in the upper troposphere and lower stratosphere increases with height (e.g., Wang et al., 2020). The climate-induced changes in ozone STEs associated with GHG/SST changes thus include the impacts of changes in BDC, ozone chemistry, and fitted isentropic surface height. Figure 12 shows the trends of ozone mixing ratio at the fitted upper isentrope averaged over the NH and SH extratropics and tropics for both 1960–2000 and 2000–2100, due to GHG/SST, ODS, and "other" changes, where GHG/SST effects are separated into those due to GHG/SST-induced BDC&Chemistry changes, and those due to fitted isentropic surface height changes. See Appendix D for the two methods used to separate the effects of BDC&Chemistry and fitted isentrope height changes. Similar results are obtained using the two methods (Figure S4 in Supporting Information S1), and the results from the first method are shown in Figure 12.

As expected, increased fitted isentrope heights lead to increased ozone concentrations there over all regions (Figure 12). In the extratropics, the BDC&Chemistry lead to increased ozone concentrations for 1960–2000 and 2000–2099, with larger magnitudes for 1960–2000. Interestingly, the BDC&Chemistry effects in the extratropics are slightly larger than the isentrope effects for 1960–2000, but smaller for 2000–2099 (Figures 12a and 12c vs.

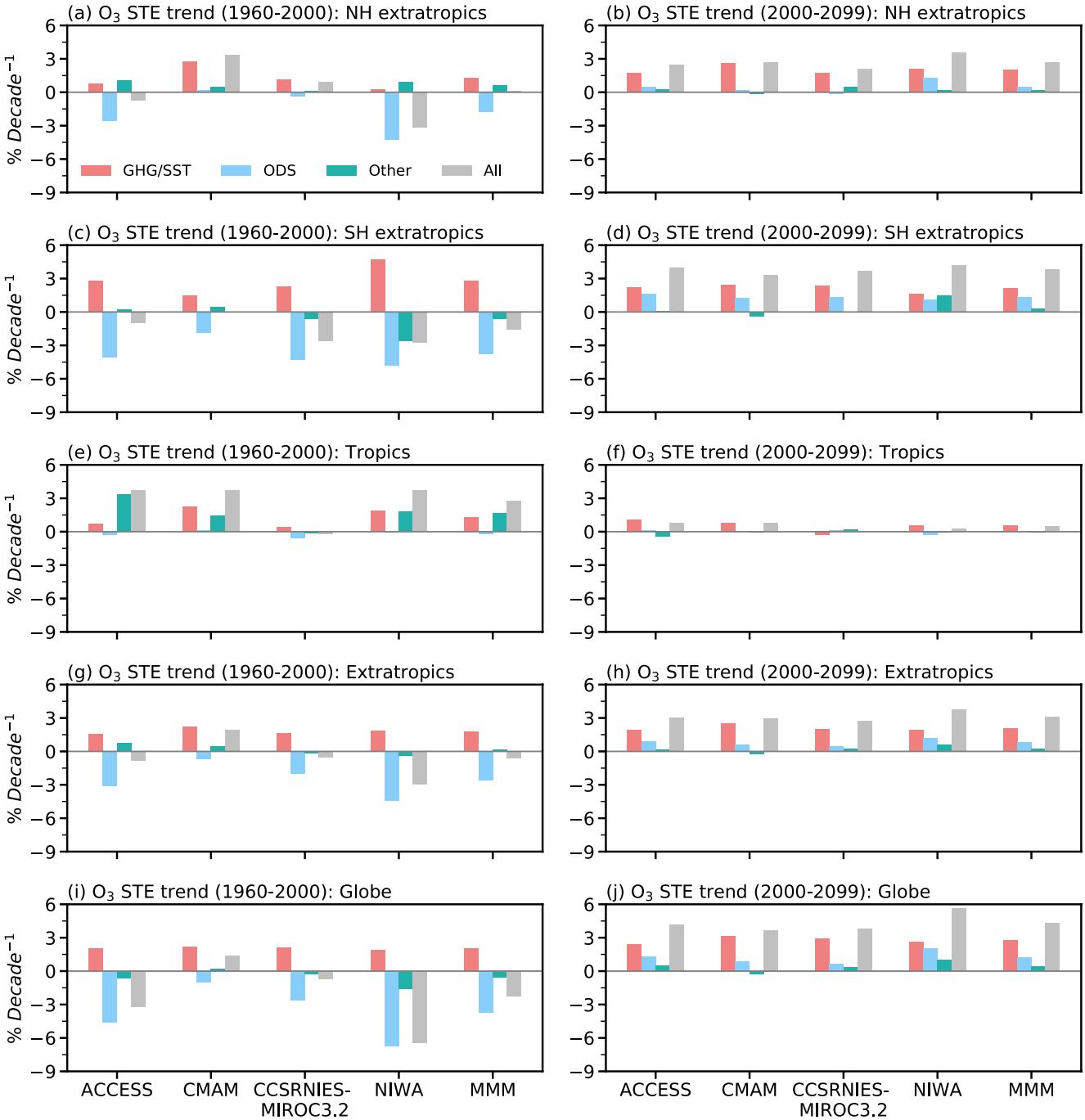

Figure 11. The trends of tropopause net ozone fluxes (gray), that is, ozone stratosphere-troposphere exchange (STE), for 1960–2000 (left) and 2000–2099 (right), and the trends due to changes in greenhouse gases and sea surface temperatures (GHG/SST, pink), ozone-depleting substances (ODS, blue), and other (green) in (a–b) the Northern Hemisphere extratropics, (c–d) Southern Hemisphere extratropics, (e–f) tropics, (g–h) extratropics, and (i–j) the globe for the four individual model and the multi-model mean (MMM) of the four models. The trends' units are in % decade^{-1}, which are the ozone flux trends scaled by the corresponding REF-C2 climatological values over 1980–2020.

Figures 12b and 12d). In the tropics, the BDC&Chemistry and isentrope effects are in opposite signs, as expected. For 1960–2000, the increased ozone concentrations due to GHG/SST are more dominated by the isentrope effect (Figure 12e). On the other hand, the BDC&Chemistry and isentrope height effects over the tropics for 2000–2099 more cancel each other (Figure 12f).

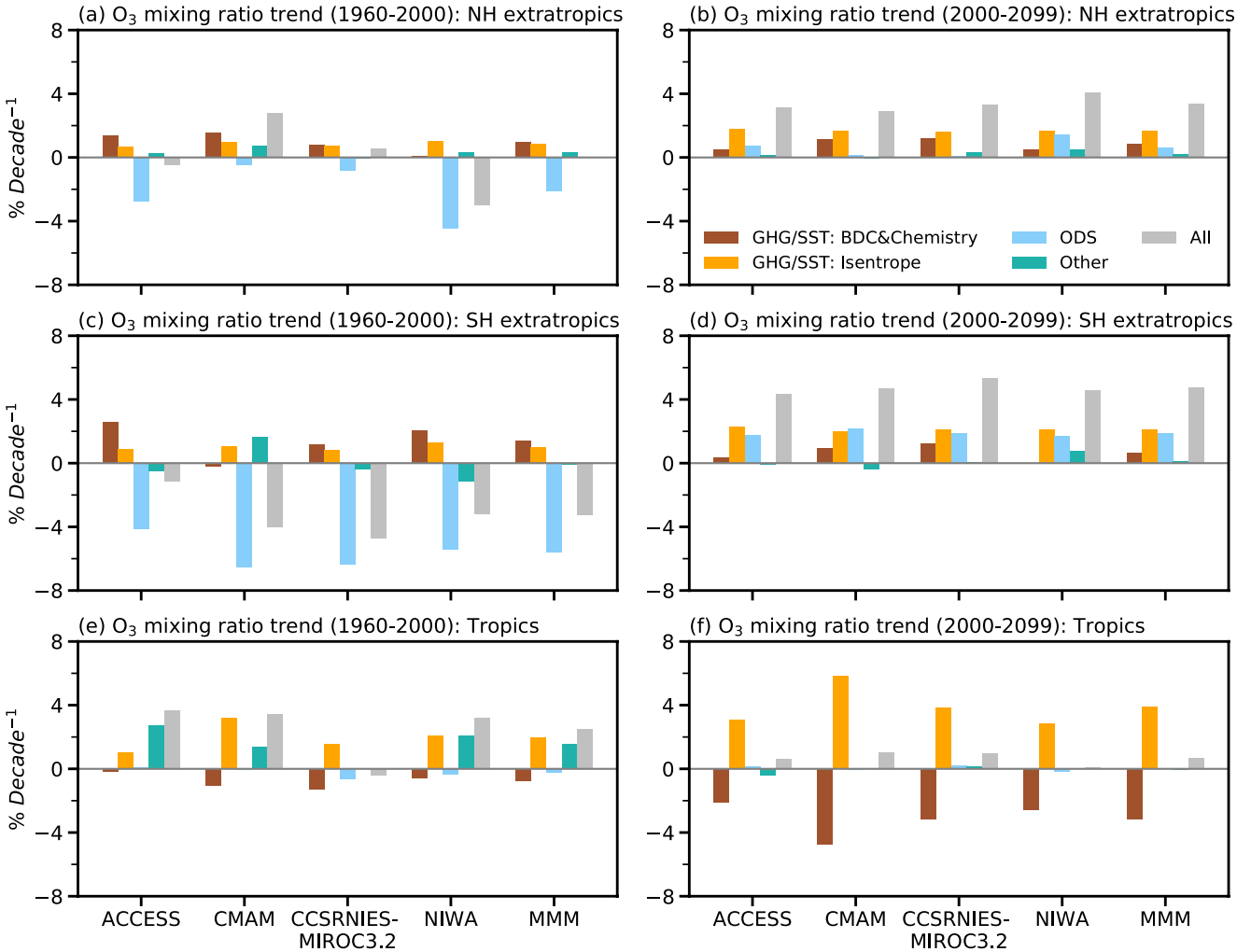

Figure 12. The trends of ozone mass mixing ratio at the fitted upper isentrope (gray), averaged over (a–b) the Northern Hemisphere extratropics, (c–d) Southern Hemisphere extratropics, and (e–f) tropics for 1960–2000 (left) and 2000–2099 (right), and the trends due to greenhouse gases and sea surface temperatures (GHG/SST)-induced BDC&Chemistry (brown) and upper isentrope height (orange) changes, ozone-depleting substance (ODS, blue) change, and other changes (green) for the four individual model and the multi-model mean (MMM) of the four models. The trends' units are in % decade^{-1}, which are the ozone mass mixing ratio trends scaled by the REF-C2 climatological values over 1980–2020.

Recently Match and Gerber (2022) used multiple chemistry-climate model experiments and an idealized model to disentangle the impacts of BDC strengthening and tropical expansion on the tropical lower stratospheric ozone. They argued that under global warming, along with strengthening upwelling, tropospheric expansion contributes at a leading order to the tropical lower stratospheric ozone reduction. In particular, Match and Gerber (2022) showed that the tropical lower-stratospheric ozone concentration at a given height decreases due to a lifting of tropical tropopause. If this is the case, the "BDC&Chemistry" effects in the tropics shown in Figures 12e and 12f should also include the impact of tropospheric expansion under global warming, which reduces tropical lower stratospheric ozone (Match & Gerber, 2022). A further separation of the tropical expansion contribution from the BDC and ozone chemistry effects requires an interventional approach such as that used by Match and Gerber (2022), which is out of the scope of the current study. Note that the "Isentrope" effect shown in Figure 12 is specifically for the ozone concentration changes at the fitted isentropic surface due to a higher fitted surface in a warming world, for the given ozone climatology field (Appendix D). The "Isentrope" effect is positive as expected (Figure 12), which does not include the tropospheric expansion impact for a given height. It is worth pointing out that the ozone change that we are interested in here is at a dynamic level relative to the tropical tropopause instead of at a given level (e.g., a given height) as in Match and Gerber (2022).

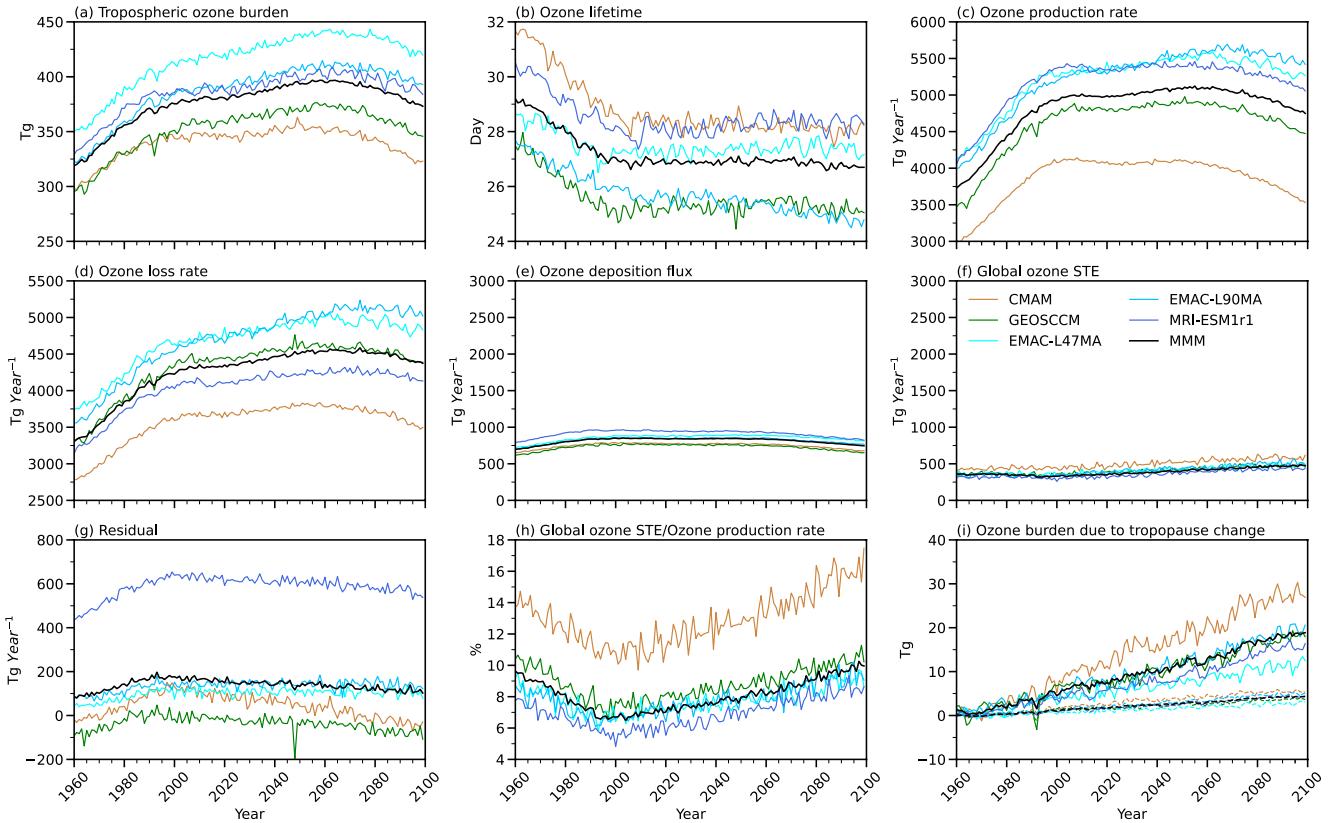

Figure 13. Time series of (a) global annual-mean tropospheric ozone burden, (b) ozone lifetime, (c) ozone production rate, (d) ozone loss rate, (e) ozone deposition flux, (f) global ozone stratosphere-troposphere exchange (STE), (g) the residual of tropospheric ozone budget (i.e., the residuals of tropospheric ozone sources minus the ozone sinks), (h) the ratio between global ozone STE and tropospheric ozone production rates, and (i) tropospheric ozone burden due to tropopause change between 1960 and 2099. Black lines are the multi-model mean results. Note that the sign of global ozone STE is changed to positive in (f). In (i), the solid and dashed lines represent the upper and lower bounds of our estimates, respectively (see the text for the details).

6. Tropospheric Ozone Budget

Figure 13 shows the time series of tropospheric ozone burden, tropospheric ozone lifetime, ozone production rate, ozone loss rate, ozone deposition, global ozone STE, ozone budget residual, the ratio of global ozone STE to ozone production rate, and tropospheric ozone burden change due to tropopause changes, which can be derived from the outputs of five CCMI models (Table S1 in Supporting Information S1). The MMM here is the mean of these five models. The ozone lifetime is the tropospheric ozone burden divided by the ozone sinks (i.e., the summation of ozone loss rate and dry deposition). The residual is the difference between total ozone sources (i.e., chemical production and global ozone STE) and total ozone sinks (i.e., chemical loss and deposition). Note that the sign of global ozone STE is changed to positive in Figure 13f.

As shown in Figure 13a, all models show that the tropospheric ozone burdens increase quickly until 2000, then increase at a slower rate until 2060, and decrease afterward. The large increases in tropospheric ozone burden for 1960–2000 agree with previous studies (e.g., Revell et al., 2015; Young et al., 2013). Tropospheric ozone burden changes are likely due to changes in GHG and ozone precursor emissions, for example, methane and nitrogen oxides (Abalos et al., 2020; Meinshausen et al., 2011). The tropospheric ozone lifetime decreases for 1960–2000, then remains unchanged for 2000–2099 (Figure 13b). Like the tropospheric ozone burden, the magnitudes of ozone production rate, loss rate, and deposition flux increase quickly until 2000, then increase at much smaller rates until 2060, and decrease afterward (Figures 13c and 13e). The magnitudes of ozone STEs are relatively small compared to ozone production and loss rates (Figure 13f). Most models have residuals ranging from −100 to 200 Tg year^{-1}, except for the MRI-ESM1r1, which has a residual of up to 600 Tg year^{-1} (Figure 13g). Note that the CCMI outputs of tropospheric ozone production and loss rates only include the major reactions, which may partly be responsible for the non-zero residuals of the tropospheric ozone budget. The non-zero residuals

may also be related to the simplified tropospheric chemistry implemented in CCMI models (see Morgenstern et al., 2017) and the fast chemical cycles between ozone and hydrogen oxide (Bates & Jacob, 2020). The ratios between global ozone STE and ozone production rates decrease for 1960–2000 and then increase for 2000–2099, indicating that global ozone STEs play a more important role in the past and future climates as compared to the current, for example, 1980–2020 (Figure 13h).

As the tropopause height increases in a warming world, tropospheric air mass also increases. Thus, in addition to the tropospheric ozone chemistry, surface deposition, and ozone STE, the tropospheric ozone burden might also change with the tropopause. To quantify this effect, we first derive the tropopause monthly anomalies in REF-C2 from 1960 to 2099, relative to the monthly climatology in the first six years over 1960–1965. The tropospheric ozone burden anomalies due to tropopause anomalies are then obtained by multiplying the tropospheric column air mass anomalies with the corresponding tropopause monthly ozone mass mixing ratio for 1960–2099. Here it is assumed that the ozone concentrations within the increased tropospheric column due to lifting tropopause are those at the tropopause, which represents an upper bound of estimates. We also derive the tropospheric ozone burden anomalies due to tropopause anomalies by multiplying the tropospheric column air mass anomalies with the corresponding monthly ozone mass mixing ratio at 500 hPa for 1960–2099. Here it is assumed that ozone concentrations associated with the increased tropospheric column due to lifting tropopause are the tropospheric values, representing a lower bound of estimates. The results are shown in Figure 13i. With the increased tropopause heights from 1960 to 2099 (Figure 1a), the MMM tropospheric ozone burden increases by 4.2–18.4 Tg, which is about 1%–5% of the total tropospheric ozone burden.

7. Discussions

The strengthening of ozone STEs in a warming world from this study agrees with previous studies (e.g., Abalos et al., 2020; Collins et al., 2003; Hegglin & Shepherd, 2009; Hess et al., 2015; Meul et al., 2018). Using the lowermost stratosphere mass budget approach with a fixed 100 hPa upper boundary and residual vertical velocity, Hegglin and Shepherd (2009) derived ozone STE based on three-ensemble CMAM simulations under the IPCC A1B emissions scenario. As in many previous studies using the lowermost stratosphere mass budget approach, the upward ozone fluxes in the deep tropics are neglected in their global ozone STE calculations (Wang et al., 2022). Hegglin and Shepherd (2009) showed that ozone STE increased by 23% for 1965–2095 (i.e., a trend of 1.8% decade^{-1}) as a result of climate change. Such a result is quite close to our estimates of ozone STEs trends due to GHG/SST changes over the extratropics, with the MMM trends of 1.8% decade^{-1} for 1960–2000 and 2.1% decade^{-1} for 2000–2099 (see pink color bars in Figures 11g and 11h). But it is somewhat smaller than our global ozone STE trends of 2.1% for 1960–2000 and 2.7% for 2000–2099 (see pink color bars in Figures 11i and 11j). A global ozone STE relative trend is smaller than that over the extratropics partly because the global ozone STE climatology magnitude of 340 Tg year^{-1} (Table 1) is smaller than the extratropical 478 Tg year^{-1}, meaning a smaller denominator magnitude when deriving the relative trend. An agreement over extratropics between our results and the results of (Hegglin and Shepherd (2009) is encouraging but may happen by chance. With a fixed 100 hPa as the upper boundary of the lowermost stratosphere (Hegglin & Shepherd, 2009), higher tropopause heights in warming climates would lead to the poleward shift of the equatorward boundaries of their region over which the ozone STE was estimated. It would thus lead to an apparent increase in the net downward ozone fluxes over the region considered, because fewer tropical upwelling portions are included (see Section 3 in Wang et al., 2022 for more details). On the other hand, the ozone STE trend may also be affected by different emission scenarios (i.e., IPCC A1B with an effective radiative forcing of 6.05 W m^{-2} in 2100, vs. RCP 6.0 with an effective radiative forcing of 5.15 W m^{-2} in 2100) and different models used. It is also noted that the region over which the ozone STE was examined by Hegglin and Shepherd (2009), which includes part of the tropics but misses the deep tropics, is different from both the extratropics and global coverage in this study (Appendix B).

Using a fixed upper boundary of 91 hPa for the lowermost stratosphere, Meul et al. (2018) investigated future ozone STEs and separated the GHG/SST and ODS effects based on EMAC model simulations. As in Hegglin and Shepherd (2009), the upward ozone fluxes in the deep tropics are neglected in their global ozone STE estimates. For 1960–2000, their ozone STE trend is −0.76% decade^{-1}, which is within our CCMI range from −5.7% to 1.9% decade^{-1} in the extratropics (Figure 3o). For 2000–2100, Meul et al. (2018) showed the ozone STE trend was 4.2% decade^{-1} under the RCP6.0 scenario, which is again within our CCMI estimates over the extratropics, ranging from 2.7% to 6.6% decade^{-1} (Figure 3p). It is noted that our MMM ozone STE relative trend magnitude

over the extratropics (i.e., for −0.9% decade^{-1} in 1960–2000 and 3.5% decade^{-1} in 2000–2099) is smaller than that over the globe (i.e., for −2.7% decade^{-1} in 1960–2000 and 4.7% decade^{-1} in 2000–2099) (see Table 1). It is also worth noting that the trends in this study are scaled by the 1980–2020 climatology, and the magnitudes of relative trends from 2000 to 2099 would become smaller if scaled by mean values over 2000–2099.

Using multiple CCMI model simulations and the stratospheric ozone passive tracers (i.e., O_3S), Abalos et al. (2020) found that the stratospheric ozone in the troposphere was projected to increase by 10%–16% (i.e., trends of 1%–1.6% decade^{-1}) by the end of the 21st century in the RCP6.0 scenario. Note that the relative trends in stratospheric ozone amount (Tg) from Abalos et al. (2020) should not be directly compared with the relative trends in ozone STE rate (Tg year^{-1}). This is especially the case by considering that the magnitudes of ozone STEs are relatively small compared to the ozone chemical production and loss rates (see Figure 13). The ozone STE changes shown in this study might not be expected to lead to the same relative changes in the stratospheric ozone amount in the troposphere as shown in Abalos et al. (2020). Bates and Jacob (2021) introduced an expanded odd oxygen family to track the contributions of different ozone sources, which could be a useful tool to quantify the ozone STE contribution to the tropospheric ozone burden change, but it is out of the scope of the current study.

8. Conclusion

This study investigates air mass and ozone STEs using CCMI model simulations from 1960 to 2099 under a climate change scenario (RCP6.0). Contrary to previous studies using a fixed upper boundary of the lowermost stratosphere, we employ a lowermost stratosphere mass budget approach with a dynamic isentropic surface fitted to the tropical tropopause as the upper boundary of the lowermost stratosphere (Wang et al., 2022). In addition, we estimate the STEs of air mass and ozone concentrations over the extratropics, tropics, and globe. The contributions to the air mass and ozone STE changes from GHG/SST and ODS changes are quantified.

The changes in air mass STEs in CCMI models for 1960–2000 and 2000–2099 are all small (within 0.3% and 0.1% decade^{-1}, respectively) over all regions, with either positive or negative signs. This is due to the cancellation between increased magnitudes of diabatic heating related to the BDC strengthening and decreased isentropic density due to higher fitted upper isentrope. The MMM of ozone STE trends for 1960–2000 are 0.3%, −2.7%, 3.4%, −0.9%, and −2.7% decade^{-1} over the NH extratropics, SH extratropics, tropics, extratropics, and globe, respectively. The corresponding MMM ozone STE trends for 2000–2099 are 3.0%, 4.3%, 0.8%, 3.5%, and 4.7% decade^{-1}. The changes in ozone STEs in both 1960–2000 and 2000–2099 are dominated by ozone concentration changes. For 1960–2000, the small ozone STE changes in the NH extratropics are due to the cancellation between GHG/SST and ODS effects, while the large decreases in ozone STEs in the SH extratropics are dominated by ozone depletion caused by ODS. More ozone is transported from the tropical troposphere to stratosphere for 1960–2000 largely due to increased tropospheric ozone. A decreased global ozone STE magnitude for 1960–2000 was caused by ODS-induced ozone loss that is partly compensated by climate-induced ozone changes. For 2000–2099, we find about one-third of global ozone STE increases are caused by the ozone recovery due to the phaseout of ODS, while two-thirds are due to increased ozone concentrations in the lower stratosphere due to GHG/SST effects through a strengthening of BDC, reduced stratospheric ozone destruction related to the temperature-dependent Chapman reaction, and upward shift of the upper boundary of the lowermost stratosphere.

Finally, we show that ratios between the global ozone STE and the tropospheric ozone production rates are decreased for 1960–2000 but increased for 2000–2099, indicating ozone STEs play a more important role in the tropospheric ozone budget in the past and future climates compared to the current climate.

Appendix A: Lowermost Stratosphere Mass Budget Approach With Dynamic Upper Isentrope

A schematic of the dynamic upper isentrope method of Wang et al. (2022) is shown in Figure A1. Contrary to the use of a constant 380 K isentrope, the dynamic upper isentrope (red solid line in Figure A1) is determined for each month by minimizing the difference between an isentrope and the lapse-rate tropopause over the tropics that is equatorward of the latitudes with zero tropopause diabatic heating. The results remain similar if we derive the dynamic upper isentrope annually by fitting the isentrope to the annual-mean tropical lapse-rate tropopause (not shown). In the dynamic upper isentrope method, the tropics/extratropics boundaries are defined as the latitudes with zero diabatic heating at the fitted upper isentrope. The fitted isentropic surface in the tropics is

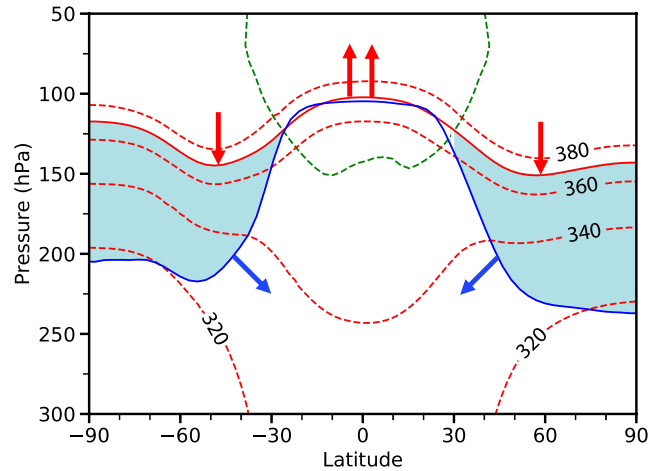

Figure A1. Schematic diagram of the stratosphere-troposphere exchange of air masses and ozone concentrations in the dynamic upper isentrope method. The green dashed line is the zero diabatic heating contour, and the blue solid line is the lapse-rate tropopause. The red solid line is the isentropic surface fitted to the tropopause over the tropics that is equatorward of the latitudes with zero tropopause diabatic heating. In the dynamic upper isentrope method, the tropics/extratropics boundaries are defined as the latitudes at the fitted isentrope with zero diabatic heating. The fitted isentropic surface serves as the upper boundary of the extratropical lowermost stratosphere (light blue shaded regions), while the tropical tropopause is approximated by the fitted isentropic surface. Blue arrows indicate the tropopause net fluxes in the extratropics, and the downward and upward red arrows indicate the diabatic fluxes across the upper isentrope in the extratropics and tropics, respectively. The isentropic surfaces of 320, 340, 360, and 380 K are shown as red dashed lines.

used to approximate the tropical lapse-rate tropopause. The tropopause is then the combination of the lapse-rate tropopause in the extratropics and the fitted upper isentrope in the tropics. Note that Wang et al. (2022) used the 3.5 PVU tropopause over the extratropics. The regions poleward of zero diabatic heating latitude at the fitted upper isentrope are the extratropics (blue shading in Figure A1), and the equatorward regions are the tropics. The summation of fluxes over the NH and SH extratropics is referred to as the flux over the extratropics, and the flux over the globe is the summation of the fluxes over the extratropics and tropics. The flux over the globe is insensitive to the definition of tropical boundaries (Wang & Fu, 2021).

The diabatic flux across the fitted upper isentrope, F_{upper}, over the NH extratropics, SH extratropics, and tropics is

$$F_{\text{upper}} = \iint Q\sigma \, dA \tag{A1}$$

where $Q = R\frac{\theta}{T}$ is the diabatic heating rate, $\sigma = -g^{-1}\frac{\partial p}{\partial \theta}$ is isentropic density, R is the radiative heating rate, θ is the potential temperature, T is the temperature, p is pressure, g is the gravitational acceleration constant, and A is the area at the fitted isentropic surface in the NH extratropics, SH extratropics, and tropics.

Following Appenzeller et al. (1996), the net air mass flux across the tropopause (F_{trop}) over NH/SH extratropics can be derived from the sum of the diabatic flux across the fitted upper isentrope (F_{upper}) and the lowermost stratosphere air mass change rate ($\frac{dM}{dt}$),

$$F_{\text{trop}} = F_{\text{upper}} + \frac{dM}{dt} \tag{A2}$$

where the lowermost stratosphere air mass, M, is from

$$M = \iiint_{P_i}^{P_t} 1/g \, dpdA \tag{A3}$$

in which P_t and P_i are pressures at the tropopause and fitted isentropic levels, respectively. In the tropics, $F_{\text{trop}} = F_{\text{upper}}$.

Similarly, the diabatic ozone flux at the fitted upper isentropic surface, $F_{\text{upper}}^{O_3}$, is determined by

$$F_{\text{upper}}^{O_3} = \iint Q\sigma q_{O3} dA \tag{A4}$$

where q_{O3} is the ozone mass mixing ratio. The net ozone flux across the tropopause ($F_{\text{trop}}^{O_3}$) over NH/SH extratropics can be calculated from the diabatic ozone flux at the fitted upper isentropic surface ($F_{\text{upper}}^{O_3}$) and the rate of change of ozone mass in the lowermost stratosphere $\left(\frac{dM_{O_3}}{dt}\right)$,

$$F_{\text{trop}}^{O_3} = F_{\text{upper}}^{O_3} + \frac{dM_{O_3}}{dt} \tag{A5}$$

where the lowermost stratospheric ozone mass, M_{O_3}, is

$$M_{O_3} = \iiint_{P_i}^{P_t} q_{O_3}(p)/g \, dpdA \tag{A6}$$

in which $q_{O_3}(p)$ is the ozone mass mixing ratio at every pressure level within the lowermost stratosphere. In the tropics, $F_{\text{trop}}^{O_3} = F_{\text{upper}}^{O_3}$. Note that, contrary to Wang et al. (2022), we neglect the ozone net chemical source in the lowermost stratosphere (CTO3) in Equation A5. That is because only half of the 10 models (see Table S1 in Supporting Information S1) provide ozone chemical production and loss terms. In addition, ozone chemical production and loss terms from the CCMI models do not include the reactions involving the ODS (e.g., chlorine-related ozone loss reactions). More importantly, the magnitudes of CTO3 in the lowermost stratosphere are quite small, including over the SH extratropics (not shown).

In the above equations, F_{upper} is positive (negative) for the upwelling (downwelling) flux. F_{trop} is negative for the flux entering the troposphere in the extratropics and positive for the flux entering the stratosphere in the tropics. More details can be found in Wang et al. (2022).

It is noted that the annual mean $\frac{dM}{dt}$ in Equation A2 and $\frac{dM_{O_3}}{dt}$ in Equation A5 are negligibly small as compared to the annual mean tropopause net air mass and ozone fluxes, respectively. For instance, the MMM annual mean $\frac{dM}{dt}$ ($\frac{dM_{O_3}}{dt}$) climatology for 1980–2020 is -0.04×10^9 kg s^{-1} (-3.9 Tg year^{-1}) in the NH extratropics and 0.05×10^9 kg s^{-1} (-0.5 Tg year^{-1}) in the SH extratropics, corresponding to 0.4% (1.4%) of the MMM annual-mean tropopause net air mass (ozone) flux climatology in the NH extratropics and -0.6% (0.2%) in the SH extratropics. In addition, the MMM $\frac{dM}{dt}$ ($\frac{dM_{O_3}}{dt}$) trend magnitude for both 1960–2000 and 2000–2099, scaled by the MMM annual-mean tropopause net air mass (ozone) flux climatology, is within 0.02% decade^{-1} (0.1% decade^{-1}), which are also negligibly small. As the tropopause height increases in a warming world, so does the air mass in the troposphere, which has a mean change rate of 0.013×10^9 kg s^{-1} for 1960–2099 from MMM. At the same time, the mean change rate of air mass in the overworld is -0.011×10^9 kg s^{-1}, but the mean change rate of air mass in the lowermost stratosphere (including both NH and SH extratropics together) is close to zero. Furthermore, since the magnitude of overworld air mass change is less than 0.1% of air mass STEs over extratropics/tropics, we can justify the adjustment of the diabatic heating rate at the fitted upper isentrope to maintain a global zero net air mass flux.

Appendix B: Ozone STEs Using a Dynamic Isentrope Versus Those Using a Fixed 380 K

Tables A1 and A2 show the MMM annual-mean air mass (A1) and ozone (A2) STE climatology over 1980–2020 and the relative trends for 1960–2000 and 2000–2099, derived using a dynamic upper isentrope (Dynamic), a fixed isentrope following Appenzeller et al. (1996) (Fixed 1), a fixed isentrope following Wang and Fu (2021) (Fixed 2). In Fixed 1, the 2 PVU tropopause and a fixed isentrope of 380 K are used, and the extratropics/tropics boundaries are the cross latitudes between the 2PVU tropopause and 380 K isentrope (see Figure 1a in Wang et al., 2022). Hegglin and Shepherd (2009) and Meul et al. (2018) used a similar method but set the upper boundary of the lowermost stratosphere at a fixed pressure level of 100 and 91 hPa, respectively. In Fixed 2, the lapse-rate tropopause and 380 K isentrope are used, and the extratropics/tropics boundaries are the zero diabatic heating latitudes at the 380 K isentrope (see Figure 1b in Wang et al., 2022). Note that in Figure 1b of Wang et al. (2022),

the extratropics/tropics boundaries are the zero diabatic heating latitudes at the tropopause, but the results are quite similar using the zero diabatic heating latitudes at the 380 K isentrope (not shown). The tropopause net air mass and ozone fluxes over the extratropics and tropics from Fixed 2 include the horizontal transport across the gaps between the tropopause and 380 K between the extratropics and the tropics (Wang & Fu, 2021), which are not part of STEs.

The global ozone STE climatologies from the three methods are similar (Table A2), as expected (Wang et al., 2022). However, the ozone STE partitioning over the tropics and extratropics is different between Fixed 1 and Dynamic (Table A2). For example, the ozone STE over extratropics is −384 Tg year^{-1} from Fixed 1 but −478 Tg/year from Dynamic. This is because the extratropics in Fixed 1 include part of the tropics with upward transport (Wang et al., 2022; Wang & Fu, 2021). There are some differences between the Fixed 2 and Dynamic in the ozone STE partitioning, but they are much smaller than those between Fixed 1 and Dynamic (Table A2). The global ozone STE trends for 1960–2000 and 2000–2099 are similar among the three methods, but differences exist in the tropics and extratropics. For instance, the tropical ozone STE trends for 1960–2000 (2000–2099) are 3.4%, 5.2% and 1.7% Decade^{-1} (0.8%, 5.0%, and −1.0% Decade^{-1}) from Dynamic, Fixed1, and Fixed2, respectively. The corresponding ozone STE trends over extratropics are −0.9%, −1.8%, and −1.2% Decade^{-1} (3.5%, 4.4%, and 2.5% Decade^{-1}).

Table A1 shows large biases in estimated air mass STE climatologies and changes due to the use of a fixed isentrope. Wang et al. (2022) discussed these biases in detail (Table A2).

Table A1
Comparison of Air Mass Stratosphere-Troposphere Exchange (STE) Based on a Lowermost Stratosphere Mass Budget Approach With a Dynamic Upper Isentrope (Dynamic), a Fixed Isentrope of 380 K Following Appenzeller et al. (1996) (Fixed 1), and a Fixed Isentrope of 380 K Following Wang and Fu (2021) (Fixed 2)

	NH extratropics		SH extratropics		Tropics	
	10^9 kg s^{-1} (% decade^{-1} for 1960–2000, % decade^{-1} for 2000–2099)					
Dynamic	−9.9	(0.15, −0.04)	−8.2	**(0.32,** 0.08)	18.2	**(0.22,** −0.01)
Fixed 1	−3.4	**(3.0, 8.3)**	−2.3	**(4.8, 12.4)**	5.9	**(4.0, 9.6)**
Fixed 2	−9.0	**(1.1, 1.7)**	−7.4	**(1.3, 1.5)**	16.4	**(1.2, 1.6)**

Note. Annual mean tropopause net air mass flux climatology averaged over 1980–2020 in the Northern Hemisphere (NH) extratropics, Southern Hemisphere (SH) extratropics, and tropics are shown. The numbers in the parentheses are the corresponding relative trends (% decade^{-1}) for 1960–2000 and 2000–2099. Trend numbers shown in bold are statistically significant at a 95% confidence level following Santer et al. (2000). The multi-model mean results are shown here.

Table A2
Same as Table A1 But for Ozone STE in the Northern Hemisphere (NH) Extratropics, Southern Hemisphere (SH) Extratropics, Tropics, Extratropics, and Globe

			SH extratropics		Tropics		Extratropics			
	NH extratropics		Tg year^{-1} (% decade^{-1} for 1960–2000, % decade^{-1} for 2000–2099)						Globe	
Dynamic	−282.3	(0.3, **3.0)**	−195.6	**(−2.7, 4.3)**	137.6	**(3.4, 0.8)**	−477.9	**(−0.9, 3.5)**	−340.3	**(−2.7, 4.7)**
Fixed 1	−230.2	(−0.3, **3.7)**	−153.6	**(−4.1, 5.5)**	49.0	**(5.2, 5.0)**	−383.8	**(−1.8, 4.4)**	−334.9	**(−2.9, 4.3)**
Fixed 2	−283.1	(−0.1, **2.2)**	−202.7	**(−2.7, 2.9)**	151.0	**(1.7, −1.0)**	−485.8	**(−1.2, 2.5)**	−334.8	**(−2.5, 4.1)**

Appendix C: Longwave and Shortwave Diabatic Heating Rates

The results of longwave and shortwave diabatic heating rates are shown in Figures S1 and S2 in Supporting Information S1. No adjustment is applied to the longwave and shortwave heating rates here. The longwave heating rates are negative in the extratropics (Figures S1a and S1e in Supporting Information S1) and positive in the tropics (Figure S1i in Supporting Information S1). For 1960–2000, magnitudes of longwave cooling in the NH extratropics are increased in all models except for CNRM-CM5-3, with a MMM trend of 0.76% decade^{-1} (Figure S1c in Supporting Information S1), while the MMM trend of longwave cooling in the SH extratropics is close to zero (Figure S1g in Supporting Information S1). For 2000–2099, all models predict increased magnitudes of longwave cooling in the NH and SH extratropics (Figures S1d and S1h in Supporting Information S1). Observational and modeling studies showed that stratospheric water vapor concentrations increase with global warming (e.g., Rosenlof et al., 2001; Yue et al., 2019). The increased longwave cooling rates in the NH extratropics for 1960–2000 and 2000–2099 and in the SH extratropics for 2000-2099 may be caused by increased water vapor (e.g., Gettelman et al., 2004; Wang et al., 2022). The small changes in longwave cooling in the SH extratropics for 1960-2000 may be related to the large ozone depletion there. In the tropics, the cooling related to increased water vapor might dominate for 1960–2000 (Figure S1k in Supporting Information S1). For 2000–2099, the change in longwave heating is quite different from different models with a near-zero MMM change, indicating that the cooling related to increased water vapor and the heating due to carbon dioxide increases might be more comparable (Figures S1l in Supporting Information S1).

Shortwave heating rates are positive in all regions (Figure S2 in Supporting Information S1). For 1960–2000, all models except UMUKCA-UCAM predict increased shortwave heating rates in the NH extratropics (Figure S2c in Supporting Information S1), and all models also predict positive changes in the tropics (Figure S2k in Supporting Information S1), while no consistent changes exist in the SH extratropics (Figure S2g in Supporting Information S1). For 2000–2099, all models predict positive trends of shortwave heating rates in all regions (Figures S2d, S2h, and S2l in Supporting Information S1). Here the increased shortwave heating rates with global warming could be attributed to higher concentrations of water vapor and carbon dioxide (Gettelman et al., 2004). The volcanic eruptions of El Chichon in March 1982 and Pinatubo in June 1991, which occurred in the second period of 1960–2000, would lead to increased shortwave heating for 1960–2000. The large ozone depletion in the South pole for 1960–2000 may cancel out GHG/SST and volcanic effects in the SH extratropics. The ozone recovery for 2000–2099 would also contribute to the increased shortwave heating over the extratropics, while the ozone increases over the tropics for 1960–2000 would contribute to the positive change there, too (Figure 7).

Appendix D: Ozone Trends at the Fitted Isentrope Due To Changes in BDC and Isentropic Surface Height

We use two methods to separate GHG/SST (i.e., climate)-induced ozone trends into trends due to changes in BDC&Chemistry and trends due to fitted isentropic surface height changes for 1960–2000 and 2000–2099. In the first method, the time series of fitted upper isentrope associated with GHG/SST only for 1960–2099 is derived using the REF-C2 minus SEN-C2-fGHG fitted upper isentrope for 1960–2099 plus the SEN-C2-fODS monthly fitted upper isentrope climatology over 1960–1965. We calculate the monthly climatology of fitted upper isentrope for 1960–2000 and 2000–2099 using the time series of fitted upper isentrope associated with GHG/SST only as derived above. Ozone trends at the upper isentrope climatology are then calculated using the REF-C2 minus SEN-C2-fGHG ozone mixing ratio, which are referred to as the ozone trends due to BDC&Chemistry changes. The ozone trends due to the changes in fitted isentropic surface heights are the difference between the ozone trends due to GHG/SST and the trends due to BDC&Chemistry.

In the second method, we first obtain the ozone time series associated with GHG/SST only using the REF-C2 minus SEN-C2-fGHG ozone fields for 1960–2099 plus the SEN-C2-fODS monthly ozone climatology over 1960–1965. Same as in the first method, the time series of fitted upper isentrope associated with GHG/SST only for 1960–2099 is also obtained, from which the fitted upper isentrope trends (K decade^{-1}) for 1960–2000 or 2000–2099 are derived. We then calculate the ozone vertical gradients (units: % K^{-1}) in the isentropic coordinate for 1960–2099, using ozone fields at the fitted upper isentrope which are associated with GHG/SST only; the averaged ozone vertical gradients for 1960–2000 or 2000–2099 are then obtained. Finally, the averaged ozone vertical gradients are multiplied by the fitted upper isentrope trends to obtain ozone trends due to changes in

isentropic heights for 1960–2000 or 2000–2099. The ozone trends due to BDC&Chemistry are the difference between the ozone trends due to GHG/SST and those due to fitted upper isentrope. The ozone mixing ratio trends in the two methods are all scaled by the 1980–2020 climatology in REF-C2.

It is encouraging that the results from the two methods that might involve different underlying assumptions are very similar (Figure S4 in Supporting Information S1).

Data Availability Statement

The CCMI output data can be downloaded from the Centre for Environmental Data Analysis (CEDA): https://catalogue.ceda.ac.uk/uuid/9cc6b94df0f4469d8066d69b5df879d5 and is described by Hegglin and Lamarque (2015). The ERA5 data is downloaded from Copernicus Climate Change Service (C3S, 2017): https://cds.climate.copernicus.eu/#!/home. The MERRA-2 data used in this study are available upon request from NASA Goddard Earth Sciences Data and Information Services Center (DISC) https://disc.gsfc.nasa.gov/information/glossary?title=MERRA-2 and described by Bosilovich et al. (2015).

Acknowledgments
This research was supported by NSF Grant AGS-2202812. We would like to acknowledge high-performance computing support from Cheyenne (https://doi.org/10.5065/D6RX99HX) provided by NCAR's Computational and Information Systems Laboratory, sponsored by the National Science Foundation, for the analyses presented in this study and for data management, storage, and preservation. The authors wish to thank the International Space Science Institute (ISSI) Tropical Width Impacts on the Stratosphere (TWIST) group for the valuable discussions and feedback on this work. The authors thank Drs. Dennis L. Hartmann and K.K. Tung for valuable discussions. The authors also thank Dr. Aaron Match and two anonymous reviewers for their constructive comments that have helped improve the manuscript.

References

Abalos, M., Calvo, N., Benito-Barca, S., Garny, H., Hardiman, S. C., Lin, P., et al. (2021). The Brewer–Dobson circulation in CMIP6. *Atmospheric Chemistry and Physics*, *21*(17), 13571–13591. https://doi.org/10.5194/acp-21-13571-2021

Abalos, M., Orbe, C., Kinnison, D. E., Plummer, D., Oman, L. D., Jöckel, P., et al. (2020). Future trends in stratosphere-to-troposphere transport in CCMI models. *Atmospheric Chemistry and Physics*, *20*(11), 6883–6901. https://doi.org/10.5194/acp-20-6883-2020

Abalos, M., Polvani, L., Calvo, N., Kinnison, D., Ploeger, F., Randel, W., & Solomon, S. (2019). New insights on the impact of ozone-depleting substances on the Brewer-Dobson circulation. *Journal of Geophysical Research: Atmospheres*, *124*(5), 2435–2451. https://doi.org/10.1029/2018JD029301

Appenzeller, C., Holton, J. R., & Rosenlof, K. H. (1996). Seasonal variation of mass transport across the tropopause. *Journal of Geophysical Research*, *101*(D10), 15071–15078. https://doi.org/10.1029/96jd00821

Bates, K. H., & Jacob, D. J. (2020). An expanded definition of the odd oxygen family for tropospheric ozone budgets: Implications for ozone lifetime and stratospheric influence. *Geophysical Research Letters*, *47*(4). https://doi.org/10.1029/2019gl084486

Bosilovich, M. G., Lucchesi, R., & Suarez, M. (2015). Merra-2: File specification [Dataset]. GMAO Office Note No. 9 (Version 1.1). Retrieved from http://gmao.gsfc.nasa.gov/pubs/office_notes

Brasseur, G. P., & Solomon, S. (2006). *Aeronomy of the middle atmosphere: Chemistry and physics of the stratosphere and mesosphere*. Springer Science and Business Media.

Butchart, N. (2014). The Brewer-Dobson circulation. *Review of Geophysics*, *52*(2), 157–184. https://doi.org/10.1002/2013rg000448

Butchart, N., Scaife, A., Bourqui, M., De Grandpré, J., Hare, S., Kettleborough, J., et al. (2006). Simulations of anthropogenic change in the strength of the Brewer–Dobson circulation. *Climate Dynamics*, *27*(7–8), 727–741. https://doi.org/10.1007/s00382-006-0162-4

Chiodo, G., Polvani, L. M., Marsh, D. R., Stenke, A., Ball, W., Rozanov, E., et al. (2018). The response of the ozone layer to quadrupled CO_2 concentrations. *Journal of Climate*, *31*(10), 3893–3907. https://doi.org/10.1175/jcli-d-17-0492.1

Collins, W. J., Derwent, R. G., Garnier, B., Johnson, C. E., Sanderson, M. G., & Stevenson, D. S. (2003). Effect of stratosphere-troposphere exchange on the future tropospheric ozone trend. *Journal of Geophysical Research*, *108*(D12), 8528. https://doi.org/10.1029/2002jd002617

Cooper, O. R., Parrish, D., Ziemke, J., Balashov, N., Cupeiro, M., Galbally, I., et al. (2014). Global distribution and trends of tropospheric ozone: An observation-based reviewGlobal distribution and trends of tropospheric ozone. *Elementa: Science of the Anthropocene*, *2*. https://doi.org/10.12952/journal.elementa.000029

Copernicus Climate Change Service (C3S). (2017). ERA5: Fifth generation of ECMWF atmospheric reanalyses of the global climate. [Dataset]. Copernicus Climate Change Service Climate Data Store (CDS). Retrieved from https://cds.climate.copernicus.eu/#!/home

Fiore, A. M., Jacob, D. J., Field, B. D., Streets, D. G., Fernandes, S. D., & Jang, C. (2002). Linking ozone pollution and climate change: The case for controlling methane. *Geophysical Research Letters*, *29*(19), 25-1–25-4. https://doi.org/10.1029/2002gl015601

Fu, Q., Lin, P., Solomon, S., & Hartmann, D. L. (2015). Observational evidence of strengthening of the Brewer-Dobson circulation since 1980. *Journal of Geophysical Research: Atmospheres*, *120*(19), 10214–10228. https://doi.org/10.1002/2015JD023657

Fu, Q., Solomon, S., & Lin, P. (2010). On the seasonal dependence of tropical lower-stratospheric temperature trends. *Atmospheric Chemistry and Physics*, *10*(6), 2643–2653. https://doi.org/10.5194/acp-10-2643-2010

Fu, Q., Solomon, S., Pahlavan, H. A., & Lin, P. (2019). Observed changes in Brewer–Dobson circulation for 1980–2018. *Environmental Research Letters*, *14*(11), 114026. https://doi.org/10.1088/1748-9326/ab4de7

Fu, Q., Wang, M., White, R. H., Pahlavan, H. A., Alexander, B., & Wallace, J. M. (2020). Quasi-Biennial Oscillation and sudden stratospheric warmings during the Last Glacial Maximum. *Atmosphere-Basel*, *11*(9), 943. https://doi.org/10.3390/atmos11090943

Fu, Q., White, R. H., Wang, M., Alexander, B., Solomon, S., Gettelman, A., et al. (2020b). The Brewer-Dobson circulation during the Last Glacial Maximum. *Geophysical Research Letters*, *47*(5). https://doi.org/10.1029/2019gl086271

Gelaro, R., McCarty, W., Suárez, M. J., Todling, R., Molod, A., Takacs, L., et al. (2017). The Modern-Era retrospective analysis for research and applications, version 2 (MERRA-2). *Journal of Climate*, *30*(14), 5419–5454. https://doi.org/10.1175/jcli-d-16-0758.1

Geng, L., Murray, L. T., Mickley, L. J., Lin, P., Fu, Q., Schauer, A. J., & Alexander, B. (2017). Isotopic evidence of multiple controls on atmospheric oxidants over climate transitions. *Nature*, *546*(7656), 133. https://doi.org/10.1038/nature22340

Gettelman, A., Forster, P. M. D., Fujiwara, M., Fu, Q., Vomel, H., Gohar, L. K., et al. (2004). Radiation balance of the tropical tropopause layer. *Journal of Geophysical Research*, *109*(D7), D07103. https://doi.org/10.1029/2003jd004190

Gettelman, A., Holton, J. R., & Rosenlof, K. H. (1997). Mass fluxes of O-3, CH4, N2O and CF2Cl2 in the lower stratosphere calculated from observational data. *Journal of Geophysical Research*, *102*(D15), 19149–19159. https://doi.org/10.1029/97jd01014

Griffiths, P. T., Keeble, J., Shin, Y. M., Abraham, N. L., Archibald, A. T., & Pyle, J. A. (2020). On the changing role of the stratosphere on the tropospheric ozone budget: 1979-2010. *Geophysical Research Letters*, *47*(10). https://doi.org/10.1029/2019gl086901

Haigh, J., & Pyle, J. (1982). Ozone perturbation experiments in a two-dimensional circulation model. *The Quarterly Journal of the Royal Meteorological Society*, *108*(457), 551–574. https://doi.org/10.1002/qj.49710845705

Hardiman, S. C., Butchart, N., & Calvo, N. (2014). The morphology of the Brewer–Dobson circulation and its response to climate change in CMIP5 simulations. *The Quarterly Journal of the Royal Meteorological Society*, *140*(683), 1958–1965. https://doi.org/10.1002/qj.2258

Hegglin, M., & Lamarque, J. (2015). The IGAC/SPARC Chemistry-Climate Model Initiative Phase-1 (CCMI-1) model data output. [Dataset]. NCAS British Atmospheric Data Centre. Retrieved from https://catalogue.ceda.ac.uk/uuid/9cc6b94df0f4469d8066d69b5df879d5

Hegglin, M. I., & Shepherd, T. G. (2009). Large climate-induced changes in ultraviolet index and stratosphere-to-troposphere ozone flux. *Nature Geoscience*, *2*(10), 687–691. https://doi.org/10.1038/ngeo604

Hersbach, H., Bell, B., Berrisford, P., Hirahara, S., Horányi, A., Muñoz-Sabater, J., et al. (2020). The ERA5 global reanalysis. *The Quarterly Journal of the Royal Meteorological Society*, *146*(730), 1999–2049. https://doi.org/10.1002/qj.3803

Hess, P., Kinnison, D., & Tang, Q. (2015). Ensemble simulations of the role of the stratosphere in the attribution of northern extratropical tropospheric ozone variability. *Atmospheric Chemistry and Physics*, *15*(5), 2341–2365. https://doi.org/10.5194/acp-15-2341-2015

Hsu, J., Prather, M. J., & Wild, O. (2005). Diagnosing the stratosphere-to-troposphere flux of ozone in a chemistry transport model. *Journal of Geophysical Research*, *110*(D19), D19305. https://doi.org/10.1029/2005jd006045

Jonsson, A. I., de Grandpre, J., Fomichev, V. I., McConnell, J. C., & Beagley, S. R. (2004). Doubled CO2-induced cooling in the middle atmosphere: Photochemical analysis of the ozone radiative feedback. *Journal of Geophysical Research*, *109*(D24), D24103. https://doi.org/10.1029/2004jd005093

Kentarchos, A. S., & Roelofs, G. J. (2003). A model study of stratospheric ozone in the troposphere and its contribution to tropospheric OH formation. *Journal of Geophysical Research*, *108*(D12), 8517. https://doi.org/10.1029/2002jd002598

Li, F., Austin, J., & Wilson, J. (2008). The strength of the Brewer-Dobson circulation in a changing climate: Coupled chemistry-climate model simulations. *Journal of Climate*, *21*(1), 40–57. https://doi.org/10.1175/2007jcli1663.1

Li, F., Stolarski, R., & Newman, P. (2009). Stratospheric ozone in the post-CFC era. *Atmospheric Chemistry and Physics*, *9*(6), 2207–2213. https://doi.org/10.5194/acp-9-2207-2009

Li, F., Stolarski, R. S., Pawson, S., Newman, P. A., & Waugh, D. (2010). Narrowing of the upwelling branch of the Brewer-Dobson circulation and Hadley cell in chemistry-climate model simulations of the 21st century. *Geophysical Research Letters*, *37*(13). https://doi.org/10.1029/2010GL043718

Lin, M. Y., Fiore, A. M., Horowitz, L. W., Langford, A. O., Oltmans, S. J., Tarasick, D., & Rieder, H. E. (2015). Climate variability modulates Western US ozone air quality in spring via deep stratospheric intrusions. *Nature Communications*, *6*(1), 7105. https://doi.org/10.1038/ncomms8105

Lin, P., & Fu, Q. (2013). Changes in various branches of the Brewer-Dobson circulation from an ensemble of chemistry climate models. *Journal of Geophysical Research: Atmosphere*, *118*(1), 73–84. https://doi.org/10.1029/2012jd018813

Lin, P., Fu, Q., Solomon, S., & Wallace, J. M. (2009). Temperature trend patterns in southern hemisphere high latitudes: Novel indicators of stratospheric change. *Journal of Climate*, *22*(23), 6325–6341. https://doi.org/10.1175/2009jcli2971.1

Lin, P., Paynter, D., Ming, Y., & Ramaswamy, V. (2017). Changes of the tropical tropopause layer under global warming. *Journal of Climate*, *30*(4), 1245–1258. https://doi.org/10.1175/jcli-d-16-0457.1

Lorenz, D. J., & DeWeaver, E. T. (2007). Tropopause height and zonal wind response to global warming in the IPCC scenario integrations. *Journal of Geophysical Research*, *112*(D10). https://doi.org/10.1029/2006JD008087

Match, A., & Gerber, E. P. (2022). Tropospheric expansion under global warming reduces tropical lower stratospheric ozone. *Geophysical Research Letters*, *49*(19), e2022GL099463. https://doi.org/10.1029/2022GL099463

Meinshausen, M., Smith, S. J., Calvin, K., Daniel, J. S., Kainuma, M. L., Lamarque, J.-F., et al. (2011). The RCP greenhouse gas concentrations and their extensions from 1765 to 2300. *Climatic Change*, *109*(1), 213–241. https://doi.org/10.1007/s10584-011-0156-z

Meul, S., Langematz, U., Kröger, P., Oberländer-Hayn, S., & Jöckel, P. (2018). Future changes in the stratosphere-to-troposphere ozone mass flux and the contribution from climate change and ozone recovery. *Atmospheric Chemistry and Physics*, *18*(10), 7721–7738. https://doi.org/10.5194/acp-18-7721-2018

Molina, M. J., & Rowland, F. S. (1974). Stratospheric sink for chlorofluoromethanes: Chlorine atom-catalysed destruction of ozone. *Nature*, *249*(5460), 810–812. https://doi.org/10.1038/249810a0

Morgenstern, O., Hegglin, M. I., Rozanov, E., O'Connor, F. M., Abraham, N. L., Akiyoshi, H., et al. (2017). Review of the global models used within phase 1 of the Chemistry–Climate Model Initiative (CCMI). *Geoscientific Model Development*, *10*(2), 639–671. https://doi.org/10.5194/gmd-10-639-2017

Oberländer-Hayn, S., Gerber, E. P., Abalichin, J., Akiyoshi, H., Kerschbaumer, A., Kubin, A., et al. (2016). Is the Brewer-Dobson circulation increasing or moving upward? *Geophysical Research Letters*, *43*(4), 1772–1779. https://doi.org/10.1002/2015GL067545

Olaguer, E. P., Yang, H., & Tung, K. K. (1992). A reexamination of the radiative balance of the stratosphere. *Journal of the Atmospheric Sciences*, *49*(14), 1242–1263. https://doi.org/10.1175/1520-0469(1992)049<1242:Arotrb>2.0.Co;2

Olsen, M. A., Douglass, A. R., & Kaplan, T. B. (2013). Variability of extratropical ozone stratosphere-troposphere exchange using microwave limb sounder observations. *Journal of Geophysical Research: Atmosphere*, *118*(2), 1090–1099. https://doi.org/10.1029/2012jd018465

Olsen, M. A., Schoeberl, M. R., & Douglass, A. R. (2004). Stratosphere-troposphere exchange of mass and ozone. *Journal of Geophysical Research*, *109*(D24), D24114. https://doi.org/10.1029/2004jd005186

Ordonez, C., Brunner, D., Staehelin, J., Hadjinicolaou, P., Pyle, J. A., Jonas, M., et al. (2007). Strong influence of lowermost stratospheric ozone on lower tropospheric background ozone changes over Europe. *Geophysical Research Letters*, *34*(7), L07805. https://doi.org/10.1029/2006gl029113

Polvani, L. M., Wang, L., Abalos, M., Butchart, N., Chipperfield, M., Dameris, M., et al. (2019). Large impacts, past and future, of ozone-depleting substances on Brewer-Dobson circulation trends: A multimodel assessment. *Journal of Geophysical Research: Atmospheres*, *124*(13), 6669–6680. https://doi.org/10.1029/2018jd029516

Revell, L. E., Tummon, F., Stenke, A., Sukhodolov, T., Coulon, A., Rozanov, E., et al. (2015). Drivers of the tropospheric ozone budget throughout the 21st century under the medium-high climate scenario RCP 6.0. *Atmospheric Chemistry and Physics*, *15*(10), 5887–5902. https://doi.org/10.5194/acp-15-5887-2015

Rosenlof, K., Oltmans, S., Kley, D., Russell, J., III, Chiou, E. W., Chu, W., et al. (2001). Stratospheric water vapor increases over the past half-century. *Geophysical Research Letters*, *28*(7), 1195–1198. https://doi.org/10.1029/2000gl012502

Rosenlof, K. H. (1995). Seasonal cycle of the residual mean meridional circulation in the stratosphere. *Journal of Geophysical Research*, *100*(D3), 5173–5191. https://doi.org/10.1029/94jd03122

Santer, B. D., Wehner, M. F., Wigley, T. M. L., Sausen, R., Meehl, G. A., Taylor, K. E., et al. (2003). Contributions of anthropogenic and natural forcing to recent tropopause height changes. *Science*, *301*(5632), 479–483. https://doi.org/10.1126/science.1084123

Santer, B. D., Wigley, T. M. L., Boyle, J. S., Gaffen, D. J., Hnilo, J. J., Nychka, D., et al. (2000). Statistical significance of trends and trend differences in layer-average atmospheric temperature time series. *Journal of Geophysical Research*, *105*(D6), 7337–7356. https://doi.org/10.1029/1999JD901105

Schoeberl, M. R. (2004). Extratropical stratosphere-troposphere mass exchange. *Journal of Geophysical Research*, *109*(D13). https://doi.org/10.1029/2004jd004525

Shindell, D. T., Faluvegi, G., Unger, N., Aguilar, E., Schmidt, G. A., Koch, D. M., et al. (2006). Simulations of preindustrial, present-day, and 2100 conditions in the NASA GISS composition and climate model G-PUCCINI. *Atmospheric Chemistry and Physics*, *6*(12), 4427–4459. https://doi.org/10.5194/acp-6-4427-2006

Skerlak, B., Sprenger, M., & Wernli, H. (2014). A global climatology of stratosphere-troposphere exchange using the ERA-Interim data set from 1979 to 2011. *Atmospheric Chemistry and Physics*, *14*(2), 913–937. https://doi.org/10.5194/acp-14-913-2014

Solomon, S. (1999). Stratospheric ozone depletion: A review of concepts and history. *Review of Geophysics*, *37*(3), 275–316. https://doi.org/10.1029/1999rg900008

Solomon, S., Garcia, R. R., Rowland, F. S., & Wuebbles, D. J. (1986). On the depletion of Antarctic ozone. *Nature*, *321*(6072), 755–758. https://doi.org/10.1038/321755a0

Solomon, S., Ivy, D., Gupta, M., Bandoro, J., Santer, B., Fu, Q., et al. (2017). Mirrored changes in Antarctic ozone and stratospheric temperature in the late 20th versus early 21st centuries. *Journal of Geophysical Research: Atmospheres*, *122*(16), 8940–8950. https://doi.org/10.1002/2017JD026719

Stohl, A., Bonasoni, P., Cristofanelli, P., Collins, W., Feichter, J., Frank, A., et al. (2003). Stratosphere-troposphere exchange: A review, and what we have learned from STACCATO. *Journal of Geophysical Research*, *108*(D12), 8516. https://doi.org/10.1029/2002jd002490

Wang, M., & Fu, Q. (2021). Stratosphere-troposphere exchange of air masses and ozone concentrations based on reanalyses and observations. *Journal of Geophysical Research: Atmosphere*, *126*(18). https://doi.org/10.1029/2021jd035159

Wang, M., Fu, Q., Solomon, S., Alexander, B., & White, R. H. (2022). Stratosphere-troposphere exchanges of air mass and ozone concentration in the Last Glacial Maximum. *Journal of Geophysical Research: Atmospheres*, *127*(10), e2021JD036327. https://doi.org/10.1029/2021JD036327

Wang, M., Fu, Q., Solomon, S., White, R. H., & Alexander, B. (2020). Stratospheric ozone in the Last Glacial Maximum. *Journal of Geophysical Research: Atmosphere*, *125*(21). https://doi.org/10.1029/2020jd032929

WMO: Scientific Assessment of Ozone Depletion. (2010). Global Ozone Research and Monitoring Project, Geneva, Switzerland, Report No. 52, 2011.

World Meteorological Organization (WMO)/United Nations Environment Programme (UNEP): Scientific Assessment of Ozone Depletion, 2006. (2007). World Meteorological Organization, Global Ozone Research and Monitoring Project, Report No. 50, Geneva, Switzerland.

Yang, H., Chen, G., Tang, Q., & Hess, P. (2016). Quantifying isentropic stratosphere-troposphere exchange of ozone. *Journal of Geophysical Research: Atmosphere*, *121*(7), 3372–3387. https://doi.org/10.1002/2015jd024180

Young, P. J., Archibald, A. T., Bowman, K. W., Lamarque, J. F., Naik, V., Stevenson, D. S., et al. (2013). Pre-industrial to end 21st century projections of tropospheric ozone from the Atmospheric Chemistry and Climate Model Intercomparison Project (ACCMIP). *Atmospheric Chemistry and Physics*, *13*(4), 2063–2090. https://doi.org/10.5194/acp-13-2063-2013

Yue, J., Russell, J., III, Gan, Q., Wang, T., Rong, P., Garcia, R., & Mlynczak, M. (2019). Increasing water vapor in the stratosphere and mesosphere after 2002. *Geophysical Research Letters*, *46*(22), 13452–13460. https://doi.org/10.1029/2019gl084973